

**INVESTIGATION OF MATISAA GRAY ROCK AS A POTENTIAL RAW  
MATERIAL FOR THE MANUFACTURE OF CEMENT**

**MWENDWA GEOFFREY MUTUA**

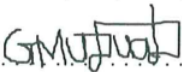
**A THESIS SUBMITTED TO THE SCHOOL OF PURE, APPLIED, AND  
HEALTH SCIENCES IN PARTIAL FULFILLMENT OF THE  
REQUIREMENTS FOR THE CONFERMENT OF MASTER OF SCIENCE  
DEGREE IN PHYSICS OF MAASAI MARA UNIVERSITY, NAROK**

**DECEMBER 2020**

## DECLARATION

I declare that this work has never been presented to any other university, college or learning institution before for academic credit or any other purpose. No article devoted to this subject has until now appeared in the professional literature. Where other people's work has been used, due acknowledgement and citation have been made.

Candidate: MWENDWA GEOFFREY MUTUA  
REG. NO.: SM03/JP/MN/3644/2017

Signature:  ..... Date: 12.06.2020 .....

Supervisor I: DR. OTIENO FREDRICK  
Department of Mathematics and Physical Sciences  
Maasai Mara University

Signature:  ..... Date: 15.06.2020 .....

Supervisor II: DR. MOTOCHI ISAAC  
Department of Mathematics and Physical Sciences  
Maasai Mara University

Signature:  ..... Date: 12-06-2020 .....

## **DEDICATION**

This work is dedicated to my parents and family.

## ACKNOWLEDGEMENTS

My sincere gratitude goes to Maasai Mara University for giving me the scholarship to pursue a master's degree. My deepest appreciation goes to my supervisors; Otieno Fredrick and Isaac Motochi for their guidance and enlightenment to undertake this research. I will forever be grateful to my mentor, Otieno Fredrick, a special friend who has always believed in me. I much appreciate Isaac Motochi for giving me the confidence to go into the academic world. Since the genesis of this work, Fredrick and Isaac have always been a prime guide to me. The discussions I had with you were informative, insightful, and truly impacting.

I started the experimental work of this research at East African Portland Cement Company Ltd. (EAPCC), Athi River), and later at the University of Nairobi (Physics Department). I am grateful to Chelimo, Sikujua, and Gabriel (EAPCC Ltd., Athi River) for allowing me access to various equipment for sample preparation and analyses. Many thanks to Justus Okonda and Moses Wabwile (University of Nairobi) for your help in Energy Dispersive X-ray Florescence (EDXRF) and Raman spectroscopy. Special thanks to Edward Tanui (Maasai Mara University) for his kindness in linking me up with EAPCC Ltd., Athi River.

I completed this thesis while at the School of Physics, University of the Witwatersrand (Wits), Johannesburg, South Africa. While at Wits University, I received untiring research support from Daniel Wamwangi. I am very grateful to Francis Otieno for his tremendous assistance in carrying out the microscopy and X-ray Diffraction (XRD) experiments and analyses. The Field Emission Electron Microscopy (FESEM) would not have been easy were it not for the help I got from Justine Sageka (University of Pretoria).

At different stages of this study, I benefited from insightful suggestions, comments, and critiques from many researchers/scholars. In particular, I would like to thank the following: Jared Ombiro, Nathan Oyaro, Aloys Osano, Stella Kirui, Wesley Omwoyo, Justus Simiyu, George Ndegwa, Samuel Muthiga, John Maera, John Matuya, and John Mining. I cannot forget to recognize my colleague researchers who in different ways contributed to achieving the objectives of the present work: Evans Suter, Tabitha Alango, Eliud Yego, Rodgers Mutisya, Evance Ouya, Sheila Jebet, John Troon, Kevin Okumu, Siololo, and Moses Kehongo. Much appreciation to Mmapula Baloi and Armand Bahini

for your assistance in learning LaTeX, the code that I used to compile my thesis. I thank Onesmus Munyithya, Nancy Kimile, Violet Kyuu, James Munywoki, Benedict Mutua, Josphine Mwikali, Peter Munywoki, Bob Mutua, Ruth Choge, Nancy Ayodi, Jacqueline Nakhulika, Augustine Kara, Abel Ithoka, Abraham Matheka, Kennie Kemboi, Victor Mutua, Raphael Namaru, Munene Mbuchi, Francis Musili and Harun Makwata for taking a keen interest in my scholarly progress.

My visits to Nairobi were filled with delight in the company of Moses Ouko, Alex Makimu, Harrison Mwinzi, Ben Ngula, Ben Muthusi, and Fredrick Musembi. I am very grateful as well for the warm friendship of Mercidonia Mbuli, Beth Kibe, Dennis Mwenda, Juliana Syuki, George Kamau, George Gatimu, Edinah Ateka, Faith Benson, Sharon Mutiso, Miriam Muthoni, Robert Mutua, Immaculate Mwanandie, and Sylvanus Kioko. Special thanks to Edwin Tallam for his inspiration and company during this work. Our nice moments of “exciting lunch” at Civic Towers, Braamfontein, cannot be forgotten. I will be eternally grateful to Bakari Chaka for his generosity, kindness, and for being a true friend.

I sincerely thank my parents Charles and Annastacia for their unceasing prayers and immense support throughout my studies. Best regards to Bob, Abel, Onesmus, Christine, Richard, Justus, Alice, and Juliana for their brotherly and sisterly concern in my studies. Special thanks to my sister, Jennifer for financial support and my brother John for assisting to excavate the samples. A great honor to John Kungú for his spiritual guidance and encouragement during the pursuit of this work.

I deeply salute my dear wife Catherine, and son Jonathan for accepting my absence for the period I have been away for studies. Your enduring patience is blessed. May the grace of God be with you always.

## ABSTRACT

Owing to the depletion rates of coastal limestone, the characterization of cementitious materials occurring on the dry land is important in order to assess their potential as alternative materials for the manufacture of cement. In this study, a naturally occurring terrestrial rock herein referred to as “Matisaa gray rock” has been studied to determine its potential for the manufacture of cement. Matisaa gray rock is found in Matisaa village, Kitui County, Kenya, and it covers an approximate area of 7 acres.

These cementitious properties were studied using X-ray fluorescence, X-ray diffraction, vibrational spectroscopy, scanning electron microscopy, micro-sieve, and Blaine techniques. Matisaa gray rock was found to contain all the oxides of cement in the following percentage abundances: 39.03 – 42.73 wt.% for CaO, 15.68 – 16.79 wt.% for SiO<sub>2</sub>, 0.47 – 4.81 wt.% for Al<sub>2</sub>O<sub>3</sub>, 0.55 – 1.04 wt.% for Fe<sub>2</sub>O<sub>3</sub>, 1.56 – 3.56 wt.% for MgO, 3.30 – 6.06 wt.% for SO<sub>3</sub>, 0.11 – 0.21 wt.% for Na<sub>2</sub>O, and 0.59 – 2.64 wt.% for K<sub>2</sub>O. Except for SO<sub>3</sub>, the proportions of the remaining oxides were found to be within the recommended thresholds.

The minerals that dominate Matisaa gray rock are dolomite (CaMg[CO<sub>3</sub>]<sub>2</sub>) and kutnohorite (Ca[Mn<sup>2+</sup>, Mg, Fe<sup>2+</sup>][CO<sub>3</sub>]<sub>2</sub>) with trace mineral phases of quartz (SiO<sub>2</sub>) and periclase (MgO). The morphology of Matisaa gray rock powder comprises of irregularly shaped particles that are compact with rough superficial texture. 69.65% of the particle size composition of Matisaa gray rock was found to be <90 μm. Out of this composition, 71.60% of the particle sizes were <45 μm, contributing to a specific surface area of 292.5 m<sup>2</sup>/kg. The high proportion of CaO and SiO<sub>2</sub> indicates that Matisaa gray rock is a silicious limestone. Its general comparison with cement properties of established raw materials of cement like Konza kunkur suggests that Matisaa gray rock has potential for utilization in the manufacture of cement.

# TABLE OF CONTENTS

<b>Declaration</b>	<b>i</b>
<b>Dedication</b>	<b>ii</b>
<b>Acknowledgements</b>	<b>iv</b>
<b>Abstract</b>	<b>v</b>
<b>Abbreviations and Acronyms</b>	<b>xiii</b>
<b>1 Introduction</b>	<b>1</b>
1.0 Background . . . . .	1
1.1 Potential Raw Materials of Cement . . . . .	2
1.2 Matisaa Gray Rock . . . . .	4
1.3 Statement of the Problem . . . . .	6
1.4 Objectives of the Study . . . . .	7
1.4.1 General Objective . . . . .	7
1.4.2 Specific Objectives . . . . .	7
1.5 Justification and Research Significance . . . . .	7
<b>2 Literature Review</b>	<b>8</b>
2.0 Introduction . . . . .	8
2.1 Cement as a Cementitious Material . . . . .	8
2.2 Tyes of Cement . . . . .	9
2.2.1 Portland Cement . . . . .	9
2.2.2 Slag Cement . . . . .	10
2.2.3 Supersulfated Cement . . . . .	11
2.2.4 Pozzolanic Cement . . . . .	11
2.2.5 High-Alumina Cement . . . . .	11
2.2.6 Expanding and Non-Shrinking types of Cement . . . . .	12
2.2.7 Gypsum types of Cement . . . . .	12
2.3 Manufacturing Cement . . . . .	12

2.4	Cement Strength . . . . .	13
2.5	Testing of Cement . . . . .	13
2.5.1	Cement Fineness . . . . .	14
2.5.2	Cement Soundness . . . . .	14
2.5.3	Cement Setting Time . . . . .	14
2.5.4	Cement Workability . . . . .	15
2.5.5	Cement Compressive Strength . . . . .	15
2.5.6	Cement Tensile Strength . . . . .	16
2.6	Composition of Standard Limestone . . . . .	16
2.7	Morphological Characteristics . . . . .	17
2.8	Particle Size Distribution . . . . .	18
2.9	Specific Surface Area . . . . .	19
<b>3</b>	<b>Theoretical Background</b>	<b>20</b>
3.0	Introduction . . . . .	20
3.1	X-ray Fluorescence . . . . .	20
3.2	X-ray Diffraction . . . . .	22
3.2.1	Bragg's condition . . . . .	22
3.2.2	X-ray Diffraction of Cementitious Materials . . . . .	24
3.3	Raman Scattering . . . . .	25
3.3.1	Classical Description of Raman Scattering . . . . .	25
3.3.2	Quantum Description of Raman Scattering . . . . .	27
3.3.3	Raman Scattering of Calcite-based Materials . . . . .	29
3.4	Raw Mix Moduli . . . . .	30
3.4.1	Hydraulic Modulus (HM) . . . . .	30
3.4.2	Lime Saturation Factor (LSF) . . . . .	31
3.4.3	Silica Ratio (SR) . . . . .	31
3.4.4	Alumina Ratio (AR) . . . . .	32
3.4.5	Sulfatisation Modulus (SM) . . . . .	32
3.5	Theory of Blaine Permeability . . . . .	33
<b>4</b>	<b>Materials and Methods</b>	<b>35</b>
4.0	Introduction . . . . .	35



4.1	Sample Preparation . . . . .	35
4.2	Characterization Techniques . . . . .	37
4.2.1	Chemical Composition . . . . .	38
4.2.2	Crystal Phase Composition . . . . .	39
4.2.3	Morphological Studies . . . . .	42
4.2.4	Particle Size Distribution . . . . .	43
4.2.5	Specific Surface Area Analysis . . . . .	43
<b>5</b>	<b>Data Presentation, Analysis, and Discussions</b>	<b>45</b>
5.0	Introduction . . . . .	45
5.1	Chemical composition . . . . .	45
5.2	Raw Mix Moduli of Matisaa gray rock . . . . .	49
5.3	Phase Identification Studies . . . . .	50
5.4	Morphological Studies . . . . .	55
5.5	Particle Size Distribution . . . . .	56
5.5.1	Specific Surface Area (SSA) . . . . .	57
<b>6</b>	<b>Summary, Conclusions, and Recommendations</b>	<b>59</b>
6.0	Introduction . . . . .	59
6.1	Summary . . . . .	59
6.2	Conclusions . . . . .	60
6.3	Recommendations for Further Study . . . . .	61
	<b>References</b>	<b>71</b>
	<b>Appendices</b>	<b>72</b>

## LIST OF FIGURES

1.1	A Map of Kenya showing the location of Matisaa area. . . . .	4
1.2	A photograph showing a section of Matisaa gray field. The general grayish appearance of Matisaa gray field is as a result of Matisaa gray rock dust. The field is characterized by shallow valleys with smoothly rising hills and sparse vegetation apart from the native sisal. . . . .	5
1.3	A photograph showing the distinct appearance of Matisaa gray field. . .	6
2.1	The structure of calcium-silica hydrate (C-S-H) (C is the Bogue notation for CaO, S for SiO <sub>2</sub> , and H for H <sub>2</sub> O) (Richardson, 2008). . . . .	9
2.2	A Flow diagram of the cement manufacturing process. The manufacture of cement requires some raw materials to be heat treated at elevated temperatures before value addition and finally grinding. . . . .	13
3.1	Schematic illustration of the principle of X-ray fluorescence. Letters K, L, and M represent the electron shells (Uo et al., 2015). . . . .	21
3.2	Bragg's condition for diffraction in real space. If the condition $2d_{hkl} \sin \theta = n\lambda$ between the incident and the scattered x-rays is satisfied, then Bragg's peaks occur at respective angles of $2\theta$ degrees. The $2\theta$ degrees scanning range of powdered materials optimizes the attainment of lattice diffraction since powders do not assume regular orientation (Le Pevelen, 2016). . . . .	23
3.3	XRD peaks representing the crystal phases of 99.2% pure limestone (Šiler et al., 2018). . . . .	25
3.4	Classical illustration of molecular vibrations in a diatomic Molecule (Schmidt et al., 2016). . . . .	26
3.5	Vibrational excitations in Raman scattering (Lohumi et al., 2017). . . . .	28
3.6	Typical spectra of Raman scattering (Lohumi et al., 2017). . . . .	29

3.7	Schematic illustration of the four vibrational modes of $\text{CO}_3^{2-}$ in calcium carbonate. (a) represent $\nu_1$ - the symmetric stretching, (b) represent $\nu_2$ - the anti-symmetric stretching, (c), represent $\nu_3$ - the in-plane bending, and (d) represent $\nu_4$ - the out-of-plane bending (Behrens et al., 2006). . . . .	30
4.1	Flow diagram showing the steps that guided the conversion of Matisaa gray rock into powder. . . . .	36
4.2	Schematic representation of the sample preparation steps: (a) As-collected sample, (b) Cleaned rock, (c) Crushed to sizes of 10 – 20 mm, (d) Pulverizing to the size of $< 1000 \mu\text{m}$ , (e) Sifted dust of micron-size particles, (f) Pelletizing to the size of 5 mm-thick and 22 mm-wide discs	37
4.3	A photograph of the EDXRF instrument (T NEX-CG “Rigaku”) that was used in this work. (Courtesy of the University of Nairobi, Kenya). The parts labelled A - shows the sample irradiation chamber, and B - vacuum pump. . . . .	38
4.4	A photograph of the WDXRF instrument (PANalytical AXIOS) that was used in this work. (Courtesy of East African Portland Cement Ltd., Athi River, Kenya). The parts labelled A - shows the sample chamber, and B - the display. . . . .	39
4.5	A photograph of the XRD equipment (Bruker D8 Discover) used in this work (Courtesy of University of the Witwatersrand, South Africa). The parts labelled A - shows the detector, B - the secondary optics, C - the sample stage, D - the copper X-ray tube, E - the primary optics, and F - the vacuum pump system. . . . .	40
4.6	A photograph of the Raman spectrometer that was used in this work. (Courtesy of the University of Nairobi, Kenya). The parts labelled A - shows the microscopy unit, and B - the light filtration unit, C - the laser unit, D - the display, and E-the central processing unit. . . . .	41
4.7	A photograph of the SEM equipment (Zeiss ULTRA Plus) that was used in this work. (Courtesy of the University of Pretoria, South Africa). The parts labelled A - shows the vacuum-pumped chamber, and B - the Gemini column hosting the beam focusing optics. . . . .	42

4.8	A photograph of the Blaine Analyzer (CM/L 0278348) that was used in this work. (Courtesy of East African Portland Cement Ltd., Athi River, Kenya). The parts labelled A - shows the sample compartment, B - the U-manometer, C - rubber bulb. . . . .	44
5.1	A bar graph showing the comparison of the elemental composition of Matisaa gray rock. . . . .	46
5.2	Comparative bar graph of the average concentration of the main cement oxides in Matisaa gray rock against those in Konza kunkur. . . . .	47
5.3	XRD spectra of Matisaa gray rock. The peak labels represent the miller indices. . . . .	51
5.4	XRD crystal phases of Matisaa gray rock. The labels D, K, P, and Q represent dolomite, kutnohorite, periclase, and quartz crystal phases respectively. . . . .	52
5.5	XRD diffractograms of Matisaa gray rock versus Konza kunkur. . . . .	53
5.6	Raman spectra of Matisaa gray rock. . . . .	54
5.7	SEM micrographs of Matisaa gray rock: (a) and (b) scanned at resolutions of 2 $\mu\text{m}$ and 200 nm respectively. . . . .	55
5.8	A comparative bar graph of particle passage analysis of Matisaa gray rock against Konza kunkur. MGR stands for Matisaa gray rock. . . . .	57
5.9	A comparative bar graph of the SSA of Matisaa gray rock against Konza kunkur cement. MGR stands for Matisaa gray rock. . . . .	58

## LIST OF TABLES

2.1	Phases of cement (wt.%) of Limestone. Data adapted from: (Liu et al., 2014) . . . . .	8
2.2	ASTM specification of the chemical composition of Portland cement (wt.%) . . . . .	10
2.3	Elemental concentration (ppm) of standard limestone. Data adapted from: (Akpan et al., 2011) . . . . .	17
2.4	Cement composition of limestone with the respective concentration (wt.%). Data adapted from: (Atiemo, 2012) . . . . .	17
5.1	Cement oxides (wt.%) in Matisaa gray rock and Konza kunkur . . . . .	47
5.2	Raw mix moduli of Matisaa gray rock and Konza kunkur. . . . .	49

## ABBREVIATIONS AND ACRONYMS

<b>MGR</b>	Matisaa Gray Rock
<b>OPC</b>	Ordinary Portland Cement
<b>HM</b>	Hydraulic Modulus
<b>LSF</b>	Lime Saturation Factor
<b>SR</b>	Silica Ratio
<b>AR</b>	Alumina Ratio
<b>SM</b>	Sulfatisation Modulus
<b>C-S-H</b>	Calcium-Silicate-Hydrate
<b>PSD</b>	Particle Size Distribution
<b>ASTM</b>	American Standard of Testing Material
<b>EDXRF</b>	Energy Dispersive X-Ray Fluorescence
<b>WDXRF</b>	Wavelength Dispersive X-Ray Fluorescence
<b>FESEM</b>	Field Emission Scanning Electron Microscope
<b>XRD</b>	X-ray Diffraction

# CHAPTER 1

## INTRODUCTION

### 1.0 Background

The need for modern-world structures is increasing in the developing world. In Kenya, the government has initiated the modern-world infrastructural development projects which are directly related to Kenya's Vision 2030. This work is devoted to the smart-city and housing pillars of Kenya's Vision 2030. These pillars are meant to raise the living standards of Kenyans to significant levels by the year 2030 (Kenya Vision 2030, 2007). Foremost, the smart-city agenda that includes but is not limited to Konza Technology City and Tatu City. Konza Technology City and Tatu City are some of the flagship projects whose establishment is envisioned to create a world-class smart city that will serve as key economic hubs in the country (Johari, 2015; Splinter & Van Leynseele, 2019).

These cities are expected to be interconnected via firm road networks, railways, and ports, just to mention a few (Government of the Republic of Kenya, 2007). Second, the housing agenda of which affordable housing is one of the four-point (The 'Big Four Agenda') main concerns singled out by His Excellency President Uhuru Kenyatta for action in pursuit of Kenya's Vision 2030 (Wanderi & Makandi, 2019). It is a kind of a mid-term plan driven to see all Kenyans in decent housing. The main material required for the implementation of these projects is cement. The raw materials availability plays a critical role in the building and construction industries by ensuring an adequate and continuous supply that maintains the production of cement. The reserves for limestone which is the main raw material of cement are facing depletion, thus necessitating the study of materials that could potentially serve as alternatives.

Shelter is considered as one of the immediate basic needs of human beings (Chavarria et al., 2014). Good shelter is not only essential but also ensures the safety and good health of the occupant. Good and durable shelter requires cement as one of the essential

raw materials. Building and construction, all hallmarks of development require cement as a primary component. However, one of the bottlenecks in the 21<sup>st</sup> century is the depletion of natural resources (Schneider et al., 2011). The cement industry is not spared from this deficiency. Limestone, the primary material for the manufacture of cement, has been depleted significantly (Rodriguez et al., 2013; Kinyua, 2013).

Most of the cementitious materials that have been explored extensively are artificially modified materials (Arvaniti et al., 2015). However, natural materials with cementitious and pozzolanic capabilities also require exploration. This is due to the technical advantages of natural cementitious materials proven in natural materials (Lothenbach et al., 2011). Moreover, natural raw materials have a broader range in mineralogical proportions and large variability in physical properties as compared to industrial by-products (Juenger et al., 2012).

Nevertheless, materials that can improve the mechanical features of concrete have shown a significant contribution towards the diversification of the natural raw materials for cement. In this regard, Matisaa gray rock has been characterized as a potential raw material that could substitute limestone in the manufacture of cement. This research was motivated by the local use of Matisaa gray rock as a gabion filler by the community living in Matisaa village. In this particular application, the fine particles of Matisaa gray rock were seen to embed in the lining of the gabion wire mesh in the presence of moisture. This property motivated the search for scientific details of Matisaa gray rock.

## **1.1 Potential Raw Materials of Cement**

Materials characterization is important in determining their appropriateness for specific applications. Cement raw materials are distinguished by the nature of their chemical composition, mineralogical phases, and some physical properties. The quality of cement raw material is dependent upon the proportion (wt.%) of the fundamental oxides (CaO, SiO<sub>2</sub>, Al<sub>2</sub>O<sub>3</sub>, Fe<sub>2</sub>O<sub>3</sub>, and MgO) (Atiemo, 2012). Each of the fundamental oxides plays a critical role in cement-based applications. For example, the content of CaO and SiO<sub>2</sub> control the hydration levels; Al<sub>2</sub>O<sub>3</sub> and Fe<sub>2</sub>O<sub>3</sub> control the pozzolanic activities,



MgO control the expansion; SO<sub>3</sub> regulate the setting time, and the alkalis (K<sub>2</sub>O and Na<sub>2</sub>O) control the corrosion (Simonsen et al., 2020).

More than 30 raw materials have been tested for their potential to manufacture cement (Worrell et al., 2001). This includes both the natural and the artificially modified materials. The vast majority of the naturally occurring raw materials of cement are of carbonate origin (Dukic et al., 2018). There are three primary types of carbonate mineralogical phases namely aragonite (CaCO<sub>3</sub>), calcite (CaCO<sub>3</sub>) and dolomite (CaMg[CO<sub>3</sub>]<sub>2</sub>) along with other non-carbonate phases like quartz (SiO<sub>2</sub>). Both calcite and aragonite are polymorphs of calcium carbonate. However, in other raw materials of cement-like sandstone, quartz is the main mineral phase (Mounia et al., 2013).

The performance of cementitious materials in concrete has been found to strongly depend on their physical characteristics and more specifically the particle size distribution (Celik, 2009). Small average particle size enhances nucleation and the pozzolanic activity of cementitious materials and therefore the strength of the resulting mixture. However, particles of the cementitious material that are smaller in size than optimal value consume more water to attain the anticipated workability, which can reduce the strength of the mixture.

In the manufacture of cement, the key features of the powders that are examined include the particle size distribution, particle shape, density, and specific surface area. Specific surface area is the general property that is applied in industrial control purposes to describe the fineness of portland cement but it does not reveal the anticipated details about the actual particle size distribution, which bears more information in resulting mixture performance (Bouyahyaoui et al., 2018). However, the particle size distribution can also be evaluated by the sieve analysis method (Dishman, 2006).

The characterization of Matisaa gray rock was based on the chemical evaluation, mineralogical composition, and physical attributes of the rock grains. The characteristics of Matisaa gray rock were compared with those of some established materials that are used by some cement manufacturing companies in Kenya. The experimental findings reported herein reveal the potential of Matisaa gray rock in the manufacture of cement as well as serving as a basis for further studies on reaction kinetics, engineering, and geological tests of Matisaa gray rock.

## 1.2 Matisaa Gray Rock

Matisaa gray rock is found in Matisaa village in Mwingi West, Kitui County, Kenya. It is a rock (in raw form) with a gray shade and hence the name “Matisaa gray rock”. Matisaa locality is located by the GPS coordinates  $1^{\circ}03'57.7''S37^{\circ}57'01.3''E$ , and approximately 150 km away from city of Nairobi. Its location on the map of Kenya is shown in Figure 1.1.

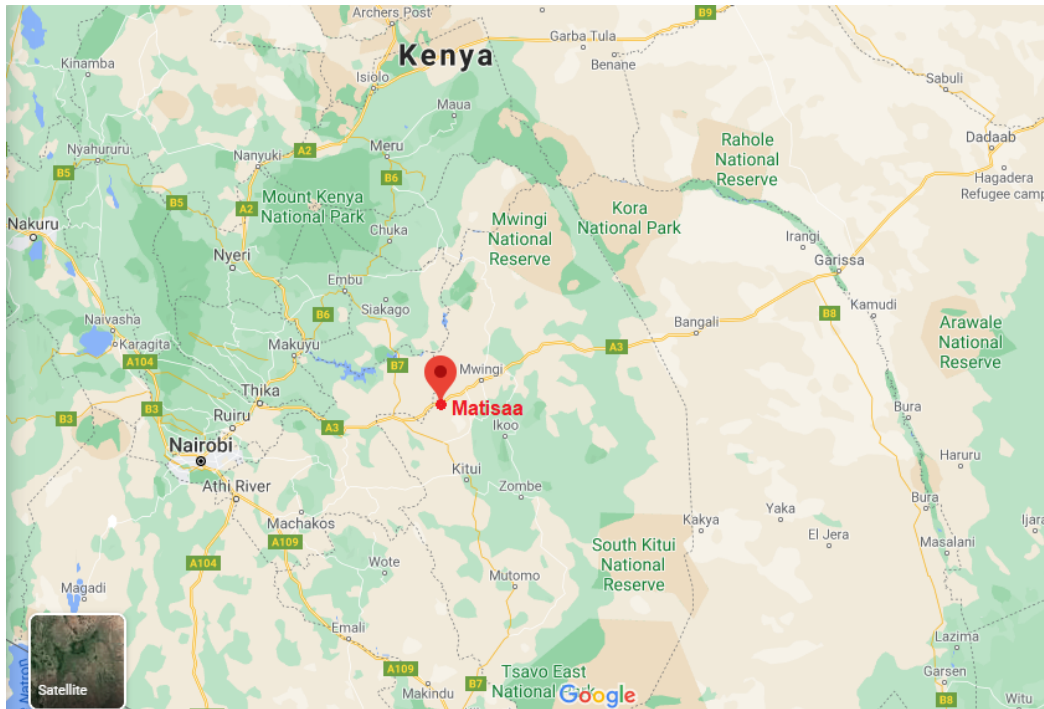


Figure 1.1: A Map of Kenya showing the location of Matisaa area.

In Matisaa, the natural scenery is characterized by distinctive high-density gray hard rocks that span the entire locality and also extend to its neighborhood. Gray rock hills and shallow valleys with smooth sides are the well-known features of Matisaa landscape. A photograph showing a section of Matisaa gray field is shown in Figure 1.2.



Figure 1.2: A photograph showing a section of Matisaa gray field. The general grayish appearance of Matisaa gray field is as a result of Matisaa gray rock dust. The field is characterized by shallow valleys with smoothly rising hills and sparse vegetation apart from the native sisal.

As shown in Figure 1.3, Matisaa gray field is distinctively marked by its grayish shade from the other general areas of Matisaa.



Figure 1.3: A photograph showing the distinct appearance of Matisaa gray field.

### **1.3 Statement of the Problem**

The cement industry is constrained in the supply of raw materials due to dwindling reserves of the available raw materials (Luo et al., 2016). A survey based on the utilization pattern of limestone predicts severe constraints in the cement industry by 2030 (Gao et al., 2015) and a bleak future by 2065 (Karstensen, 2006). Limestone, like any other non-renewable resource, has a limited supply and its pace of depletion is dependent on the utilization patterns. In view of the expected massive infrastructural development, the consumption of cement will stress the cement raw material reserves. The production capacity of cement is greatly influenced by the availability of raw materials. There is a need, therefore, to diversify the cement raw materials (Naqi & Jang, 2019) to satisfy the demand.

## **1.4 Objectives of the Study**

### **1.4.1 General Objective**

This study was carried out to investigate the potential of using Matisaa gray rock for the manufacture of cement.

### **1.4.2 Specific Objectives**

- (i) To determine the chemical and mineralogical composition of Matisaa gray rock using X-ray fluorescence and diffraction techniques
- (ii) To examine the morphological properties of Matisaa gray rock using scanning electron microscopy
- (iii) To study the particle size distribution of Matisaa gray rock.

## **1.5 Justification and Research Significance**

The demand for cement in Kenya since the year 2000 has been in an upward trend until 2018 when it fell for the first time. Even then, the fall was attributed to economic factors other than competition from cement substitutes (Kenya National Bureau of Statistics, 2018). This implies cement still plays a key role in Kenya's infrastructural development. Globally, demand for cement is forecast to expand at 1% per year further igniting interest in the search for cement raw materials such as limestone.

Due to the unlocked potential of cement raw materials in Kenya, the country (Kenya) has been importing clinker (an intermediary raw material of cement) from other countries (Mbongwe et al., 2014). The clinker imports have been approximated to 2 million tonnes every year, costing the country over 10 billion Kenya shillings annually (Capital Business, 2020). Exploiting the potential of the cement raw materials locally available in Kenya could spur the growth of the cement industry, create more jobs for Kenyans, relieve Kenya from clinker imports, reduce cement cost, create an enabling environment for Kenyans to build decent houses, thus resonating with Kenya's development blueprint.

# CHAPTER 2

## LITERATURE REVIEW

### 2.0 Introduction

This chapter gives an overview of the types of cement and cementitious materials. Their chemical and structural properties at the microscopic level are discussed. Knowledge of the chemical and microstructural behaviour of cementitious materials goes a long way in determining the application of a newly identified material. The mineralogy, morphology, and particle size distribution among various cementitious materials have been presented. The processes of manufacturing cement, as well as the tests for cement, have been discussed.

### 2.1 Cement as a Cementitious Material

Cementitious materials are composed of calcium silicate hydrates and the calcium hydroxide (portlandite). Both the calcium silicate hydrates and portlandite are mainly hydration products of tricalcium and dicalcium silicates alongside other cement phases. These phases are formed from the oxides that make up the raw materials (Jo et al., 2014). The chemical composition of cement is predominantly oxides (Alkhateeb, 2013), as shown in Table 2.1 The nomenclature of cement compounds is complex and a short-hand symbolization known as Bogue notation is therefore adopted (Abdunnabi, 2012).

Table 2.1: Phases of cement (wt.%) of Limestone. Data adapted from: (Liu et al., 2014)

Phase	Chemical Notation	Bogue Notation	Content (wt.%)
Alite	$3\text{CaO} \cdot \text{SiO}_2$	$\text{C}_3\text{S}$	64.62
Belite	$2\text{CaO} \cdot \text{SiO}_2$	$\text{C}_2\text{S}$	9.99
Aluminate	$3\text{CaO} \cdot \text{Al}_2\text{O}_3$	$\text{C}_3\text{A}$	7.33
Ferrite	$4 \cdot \text{CaO} \cdot \text{Al}_2\text{O}_3 \cdot \text{Fe}_2\text{O}_3$	$\text{C}_4\text{AF}$	8.58

The main binding phase of cement is the calcium silicate hydrates (C-S-H) (Richardson, 2008). The structure of C-S-H mainly consists of skeletal O–Si–O and O–Ca–O chains as shown in Figure 2.1.

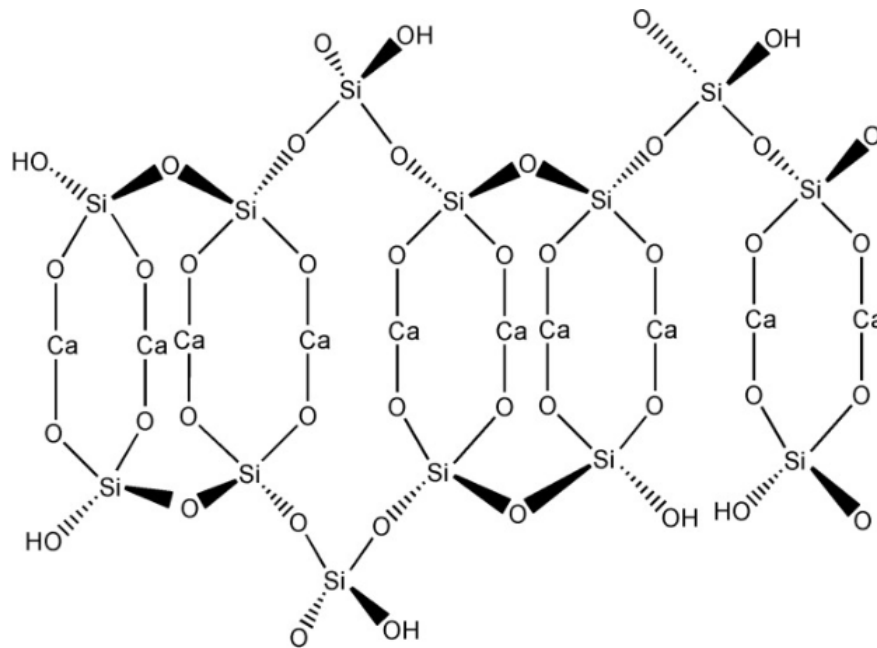


Figure 2.1: The structure of calcium-silica hydrate (C-S-H) (C is the Bogue notation for CaO, S for SiO<sub>2</sub>, and H for H<sub>2</sub>O) (Richardson, 2008).

The tetrahedral silicate chains are connected to the hexagonal skeletons of CaO which are coordinated by the octahedral Ca atoms and tetrahedral O atoms. Additionally, due to the missing tetrahedron connection, some O atoms are replaceable by OH groups.

## 2.2 Types of Cement

Cement is categorized according to the type of raw materials from which they are manufactured. They include Portland, slag, supersulfated, pozzolanic, high alumina and gypsum type of cement.

### 2.2.1 Portland Cement

Portland cement was first produced in Leeds city, England, by calcining limestone-clay mixture at 1450 °C (Dhir et al., 2017). Its name is coined from rocks that were quarried near Portland Island in the United Kingdom which resemble hardened calcined mixture of clay-limestone. The American Society for Testing and Materials categorizes portland cement as Type I (Ordinary Portland Cement), Type II (Moderate Heat of Hydration Cement), Type III (Rapid-Hardening Cement), Type IV (Low Heat Cement) and Type

V (Sulphate Resisting Cement) (Consoli et al., 2013).

These types of cement further depend on the nature of aggregates that are mixed with the clinker. Clinker is a multi-component material artificially made by pyro-fusing a mixture of limestone and clay at 1450 °C (Ahmed & Mohammed, 2012). Upon fusion, the mixture is cooled, to allow the formation of the four phases namely: alite, belite, aluminate, and ferrite. According to the British standard for cement, EN 197-1, a fine mixture of clinker (95 – 97%) and gypsum (3 – 5%) yields Portland cement.

The main component of gypsum is sulfur trioxide (Mohammed & Safiullah, 2018). The other types of cement that fall under this category include coloured and air-entraining types of cement. The chemical composition of Portland cement is as shown in Table 2.2.

Table 2.2: ASTM specification of the chemical composition of Portland cement (wt.%)

Data adapted from: (Yin et al., 2016).

Name of Oxide	Bogue Notation	Minimum	Average	Maximum
CaO	C	58.0	62.0	66.0
SiO <sub>2</sub>	S	18.0	22.0	26.0
Al <sub>2</sub> O <sub>3</sub>	A	4.0	8.0	12.0
Fe <sub>2</sub> O <sub>3</sub>	F	1.0	3.5	6.0
MgO	M	1.0	2.0	3.0
SO <sub>3</sub>	$\bar{S}$	0.5	1.5	2.5
Na <sub>2</sub> O + K <sub>2</sub> O	N + K	< 1.0	<1.0	<1.0

### 2.2.2 Slag Cement

Slag cement, which is a by-product of iron processing, is made by sudden cooling of molten iron metal to form granules which are then mixed with other suitable cement raw materials. A mixture of granulated slag and Portland cement containing up to 65% slag is known as Portland blast-furnace cement. Slag cement is rich in silica and alumina but the content of lime is lower than that of Portland cement. This makes slag cement more resistant to attack by chemicals and consequently performs well in aggressive environments (Ding et al., 2018).



### **2.2.3 Supersulfated Cement**

Supersulfated cement is an alternative category of slag-bearing cement composed of granulated slag mixed with 10 – 15% hard-calcined gypsum and 3% of Portland cement. Super-sulfated cement resembles Portland cement in strength properties, except that the former is more resistant to several types of attack in chemically active environments (Wang et al., 2016).

### **2.2.4 Pozzolan Cement**

Pozzolan types of cement are made by mixing pozzolanic materials with Portland cement (Rodríguez et al., 2013). Pozzolans that occur naturally are commonly volcanic rocks though some maybe diatomaceous. On the other hand, artificial pozzolans are the byproducts of industrial processes such as iron smelting, energy generation using coal, and other materials. Such materials include fly ash, calcined clays, and rice-husk ash. Though pozzolans are rich in silica and alumina, intrinsically they are not cementitious. However, their property that makes pozzolans cementitious when mixed with water is due to the reactive form of their chemical composition (Tutur & Noor, 2018). Pozzolan materials have proven to be effective alternatives of Portland clinker thereby creating a way for the initiation of more candidates (Mavroulidou et al., 2015).

### **2.2.5 High-Alumina Cement**

In this type of cement, a bauxite-limestone mixture is fused at 1500 – 1600 °C. The silica and magnesia contents of the limestone employed herein should be low while the bauxites should contain 50 – 60% alumina, not more than 25% iron oxide, not more than 5% silica, and 10 – 30% water of hydration. This cement contains 35 - 40% limestone, 40 – 50% alumina, up to 15% iron oxides, and preferably not more than 6% silica (Reiterman et al., 2015). The principal cementing compound in high-alumina cement is monocalcium aluminate ( $\text{CaO} \cdot \text{Al}_2\text{O}_3$ ) (Angelescu et al., 2017). High-alumina cement hardens rapidly and takes 3 days to attain an equivalent strength that takes Portland

cement 28 days (Krivoborodov & Samchenko, 2019). Due to its outstanding refractory properties, high-alumina cement with minimal proportions of iron oxide is used in linings for furnaces .

### **2.2.6 Expanding and Non-Shrinking types of Cement**

This is a blend of any of the expansive agents like alkaline silicates, sulphoaluminate, calcium aluminoferrite, magnesia, and aluminate with Portland cement. It is manufactured by calcining a blend of bauxite, chalk, and gypsum (Oye et al., 2012). The slight contractions of fresh concrete at the onset of drying are therefore counterbalanced by calcium sulfoaluminate (Sousa & Marie, 1998).

### **2.2.7 Gypsum types of Cement**

Gypsum types of cement are generated by calcining gypsum to yield calcium sulfate hemihydrate. The hemihydrate, also known as plaster of Paris, sets quickly when mixed with water and therefore a suitable protein is added in applications such as building to retard the hydration process. The primary role of gypsum in cement is to set the retardation time but it can also be optimized to improve the mechanical response and the hydration process of the cement (Mohammed & Safiullah, 2018). Gypsum types of cement are used for the manufacturing of plasterboards, slabs, and floor-surfacing.

## **2.3 Manufacturing Cement**

Cement production is a multistage process. It begins right from the excavation of the raw materials, followed by conditioning the raw meal (which is a mineral-enriching step), crushing, grinding, drying, and mixing (Uson et al., 2013). The conditioned meal is Calcined at 900 °C to decompose CaO from limestone (CaCO<sub>3</sub>). The CaO is fed in the kiln to react with SiO<sub>2</sub>, Al<sub>2</sub>O<sub>3</sub> and Fe<sub>2</sub>O<sub>3</sub> at 1450 °C. This reaction forms a mixture of silicates, aluminates, and ferrites (the clinker), which is chilled and mixed with 5% of gypsum, and finally ground to make cement (Uson et al., 2013). These steps are

summarized in the flow diagram shown in Figure 2.2.

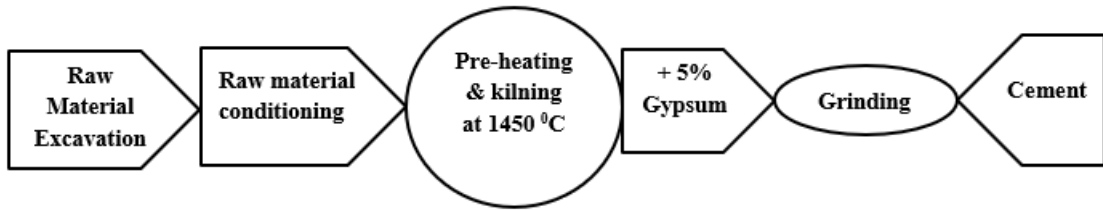


Figure 2.2: A Flow diagram of the cement manufacturing process. The manufacture of cement requires some raw materials to be heat treated at elevated temperatures before value addition and finally grinding.

## 2.4 Cement Strength

Cement strength refers to the ability of cement and its mixtures to withstand mechanical loads without failure. Compression and tensile forces are the main loads that have a critical bearing in cement applications (Chhorn et al., 2018). Like any other material, when a compression force is applied on cement, the atomic separation in the crystal planes reduces and increases on applying tension force. The alteration of the mean atomic positions leads to alteration of the bond geometry and consequently the bond strength. The net effect of these dynamics in cement is enhanced compressive strength and weak tensile strength (Cardoso et al., 2017). From a macroscopic perspective, compression forces close the voids in the bulk structure of cement thereby reducing the stress concentration zones that induce failure. When in tension, these voids open, creating more stress hotspots that trigger failure. This explains why the compressive strength of cement is way higher than its corresponding tensile strength. The tensile strength of cement is about 10–15% of the compressive strength (Park, 2003).

## 2.5 Testing of Cement

The production of cement and its final use involves the mixing of a number of ingredients and several processes. Therefore, cement must be tested to ensure compliance with specification and application-specific requirements. These tests include cement fineness, soundness, workability, setting time, compressive and tensile strengths of the cement.

### **2.5.1 Cement Fineness**

Cement fineness is a measure of the size of particles of cement. It affects the rate of cement hydration and hence strength development. Fine particles provide a large number of contacts that take part in the process of setting and hardening of the cement. Cement fineness is expressed in terms of specific surface area. It is tested using the air permeability technique (Blaine Apparatus) or calculated from particle size analysis (laser particle diffraction or micro-sieve analysis).

### **2.5.2 Cement Soundness**

Cement soundness refers to the ability of a cement paste to maintain its original volume upon setting. If expansion occurs after setting, the cement is said to be unsound. This unsoundness is caused by the presence of free CaO and high proportions of MgO (Hsu et al., 2018). The effect of unsoundness is indicated by the formation of minor cracks on the hardened cement mass. This deteriorates cement strength, and therefore the durability of cement structures. A sound cement paste is the foundation of sound cement mixtures.

A cement soundness test, known as Le Chatelier's Apparatus Test is thus conducted to find out the presence of free CaO and excess MgO. Le Chatelier's Apparatus Test is carried out by boiling the cement in water. The non-volume variation of the cement after boiling and setting signifies that the cement is sound.

### **2.5.3 Cement Setting Time**

The setting time of cement is characterized by two cycles. The first cycle, known as the initial setting time, is the time taken by cement paste to lose its plasticity. Plasticity (in the context of cement) is the ability to cast cement paste into desired molds. The initial setting time is achieved after 30 minutes for ordinary Portland cement. This cycle is important as it delays the hydration process of cement and therefore delayed hardening.

Further delay leads to loss of plasticity which translates to the loss of binding properties.

The second cycle, known as the final setting time, is the time taken by cement paste to lose its plasticity completely, that is, the paste converts into a hard solid mass. This takes 10 hours for ordinary Portland cement. Disturbances before the final setting time compromise cement structures. The setting time of cement is tested using the Vicat apparatus. The apparatus consists of a needle (Vicat needle) which is used to characterize the setting time for cement. The time taken for the Vicat needle to penetrate the cement paste into a depth of 5 mm is the initial setting time for that particular cement. The final setting time is indicated by zero penetration depth of and absence of a scratch mark by the Vicat needle on the surface of the sample. This indicates the development of sufficient strength to resist certain defined forces (Khandaker et al., 2018).

#### **2.5.4 Cement Workability**

As the name implies, workability, simply means the ‘ease to work with.’ In the context of cement, workability refers to the capacity of a cement paste or mixture to be placed and easily compacted without separating. The desired workability differs from one application to another. Cement workability is influenced by several factors such as cement composition, particle size distribution, specific surface area, and cement-water ratio, just to mention a few. There are several methods for testing cement workability. These include the Penetration Test for Segregation, Slump Flow Test, U-Box Test, J-Ring Test, V-Funnel Test, L-Box Test, Fill Box Test, and Wet Sieving Stability Test (Koehler & Fowler, 2003).

#### **2.5.5 Cement Compressive Strength**

Compressive strength refers to the ability of a material to withstand forces tending to press the material inward, thereby resisting being pushed together. This is one of the most important properties of cement mixtures. Cement and its mixtures are charac-

terized by high compressive strength, a property that makes concrete pillars ideal for supporting huge loads. The overall strength of the cement mixtures is significantly influenced by the quality of cement.

The test for compressive strength of cement is carried out using a compression machine. It involves the preparation of mortar cubes (50 mm) using cement and standard size sand in the ratio 1:3 (by mass) and a specified volume of water. The mortar cubes should cure in a manner approved by the specific standard. This strength is carried out after 3 days, 7 days, and 28 days (Zhu et al., 2012). This test is done by crushing the sample in a compression machine. The compressive strength is determined by measuring the highest stress that fractures the sample.

### **2.5.6 Cement Tensile Strength**

Tensile strength refers to the ability of a material to resist forces tending to pull it apart. Cement and its mixtures are vulnerable to tensile forces induced by temperature variations which cause. This is one reason that makes the tensile strength of cement usually lower than its compressive strength.

The test for the tensile strength of cement is carried out using a uniaxial tension machine. The sample is prepared just as for the compressive strength test. The tensile strength test is done by pulling the sample apart in a uniaxial tension machine. The tensile strength is determined by measuring the lowest force that fractures the sample.

## **2.6 Composition of Standard Limestone**

According to Akpan et al., (2011), the composition of standard limestone should be as shown in Table 2.3.

Table 2.3: Elemental concentration (ppm) of standard limestone. Data adapted from: (Akpan et al., 2011)

Element	Concentration (ppm)
Ca	562000.8
Si	272850.0
Al	60290.0
Fe	11416.0
Mg	0.0
K	2764.0
Ti	1175.4
Mn	322.4

As reported by Atiemo (2012), the cement composition of limestone should be as shown in Table 2.4.

Table 2.4: Cement composition of limestone with the respective concentration (wt.%). Data adapted from: (Atiemo, 2012)

Name of Oxide	Minimum	Average	Maximum
CaO	38.0	40.0	42.0
SiO <sub>2</sub>	20.0	22.5	25.0
Al <sub>2</sub> O <sub>3</sub>	2.0	3.0	4.0
Fe <sub>2</sub> O <sub>3</sub> +MgO+SO <sub>3</sub> +K <sub>2</sub> O+Na <sub>2</sub> O	1.5	2.0	2.5

When compared to the chemical specifications of standard limestone, low purity limestone such as dolomite are regarded as low-grade limestone (Dey et al., 2020). The utilization of such low-grade raw materials in cement manufacturing is subject to an industrial treatment known as beneficiation (Rao et al., 2009). Beneficiation refers to the incorporation of corrective additives to attain the required specifications (Rao et al., 2014). Nonetheless, the choice of the beneficiation process is influenced by several properties that mainly include the chemical, mineral and physical characteristics (Rao et al., 2011).

## 2.7 Morphological Characteristics

Morphology of cement raw materials refers to the grain shape, texture and porosity. The morphological features are important since they influence the hydration properties of cement (Yildirim & Prezzi, 2011). The morphology of raw materials of cement

differ from one material to another. For instance, the morphology of artificially modified raw materials of cement such as fly ash is characterized by broken and unbroken microspherical grains that are agglomerated. The broken microspheres comprise of sub-microspheres with hollow cavities which may be empty (cenospheres) or mineral filled (plerospheres) (Alegbe et al., 2018); (Liu et al., 2016).

The morphology of rice husk ash is characterized by cellular honeycomb-shaped grains that are porous (Trejo & Prasittisopin, 2015). Oil palm ash grain morphology is characterized by irregular and rough surfaces with porous structure (Ooi et al., 2015). These morphologies demand for high water to hydrate and attain the required workability. On the other hand, the grains of naturally occurring raw materials of cement such as limestone and sandstone are characterized by rhombohedron shapes, and thus blocky-angular and compact morphology (Gaber, 2018).

## **2.8 Particle Size Distribution**

The final process of manufacturing cement is grinding, which produces particles of different sizes. Particle size distribution is key parameter to study for a new raw material of cement as it indicates the material's energy intensiveness in addition to cement quality. Most of the energy in cement production is dedicated to particles sizing. The particle size distribution of cement is limited to 7 – 200  $\mu\text{m}$  (Zhang, 2011). However, this is centrally based on the 45  $\mu\text{m}$  and 90  $\mu\text{m}$  size proportion (CiMSA, 2017). The particle retention on the 45  $\mu\text{m}$ -sieve for natural pozzolans should be less than 34% (Arvaniti et al., 2014).

Non-threshold particle sizes are attributed to adverse effects in cement strength development, for instance, too fine particles lead to high shrinkage early hardening, whereas large particles lead to poor hydration and thus poor strength development (Zhang, 2011). The strength of cement solely depend the distribution of its particle size distribution if the mineralogical composition of cement remains constant (Gmbh, 2018).



## 2.9 Specific Surface Area

Specific surface area is the total surface area of a material per unit of mass, and it varies inversely as the particle size. It is the property that enables solids' interaction with the ambience. The specific surface area of cement is a direct consequence of its particle size. It is the main factor that influences the hydration kinetics of cement since the formation of reaction sites is favoured in the particle-water interfaces. The higher the hydration rate of cement, the higher the strength it develops. The typical values for specific surface area of Ordinary Portland cement lie between 300 – 350 m<sup>2</sup>/kg, whereas for rapid hardening Portland cement ranges between 400 – 450 m<sup>2</sup>/kg (Goncharenko et al., 2018).

Several materials have been investigated for their potential to either supplement or substitute the depleting raw materials of cement. The materials studied as supplementary are the agricultural and industrial by-products such as rice husk ash, bagasse ash, palm oil ash, fly ash, silica fume, ground granular blast-furnace slag, just to mention a few (Al-Mansour et al., 2019). However, these materials have shown little potential due to their richness in only one element (mainly SiO<sub>2</sub>), making it difficult for beneficiation. Naturally occurring terrestrial materials like sedimentary rocks and duricrusts have been studied as potential substitutes for the coastal limestone (higher grade limestone) and they have shown potential for utilization (Rao et al., 2011). However, since terrestrial materials are generally low-quality ores, their acceptance for utilization is based on the closeness of the material's proportion of the cement oxides to the specified thresholds, thus necessitating exploration of ores that meet this requirement

## **CHAPTER 3**

### **THEORETICAL BACKGROUND**

#### **3.0 Introduction**

This chapter describes the fundamental principles of light interaction with matter based on the X-ray diffraction, X-rays fluorescence, and Raman scattering. The criteria for material identification and quantification has also been described. The chapter also presents the criterion for simulation of Portland cement clinker. It ends by describing the Blaine permeability method for determining the specific surface area of powders.

#### **3.1 X-ray Fluorescence**

X-rays are electromagnetic radiations with high energy, typically ranging from 124 eV to 124 keV (Morelhão, 2016). They are produced in an evacuated tube consisting of an anode and a cathode at a high potential difference. X-ray fluorescence techniques utilize the characteristics of fluorescent x-rays to study the composition of materials. Materials naturally occur as compounds rather than pure elements. When the atoms of these compounds are bombarded with energetic incident x-rays, inelastic interaction with the atoms of the sample takes place resulting in the absorption of x-rays of specific energy. This interferes with the stability of the atoms. The atoms regain stability by re-emitting lower energy secondary x-rays (known as fluorescent x-rays). This process involves knocking out inner shell electrons and filling up the created vacancies by higher shell electrons as illustrated in Figure 3.1.

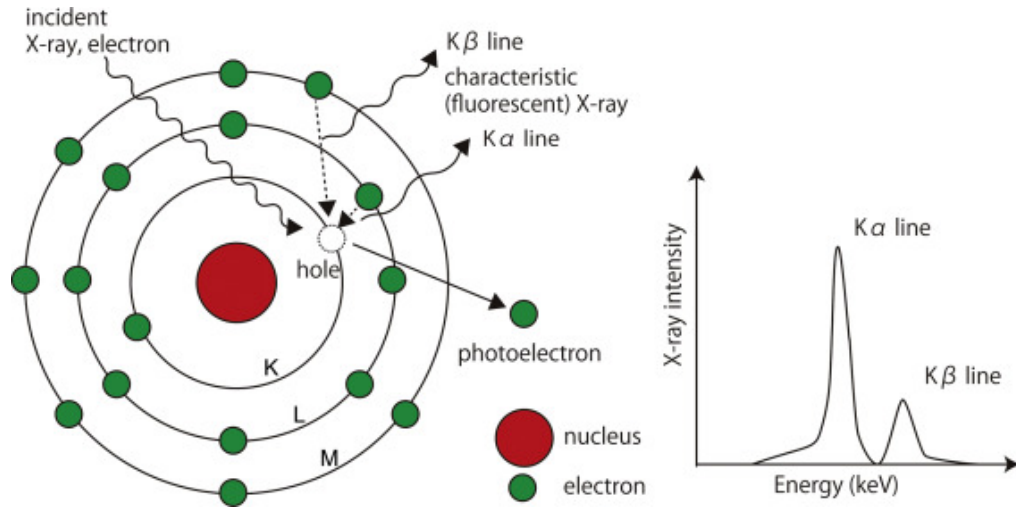


Figure 3.1: Schematic illustration of the principle of X-ray fluorescence. Letters K, L, and M represent the electron shells (Uo et al., 2015).

Each spectrum of wavelengths is a set of fingerprints for each of the minerals present in the sample. The identification of the minerals in the sample is achieved by comparing the resultant spectra characteristics against the standard reference spectra. The peak energy identifies the elements in the sample (West et al., 2012), whereas the peak height (intensity) indicates the abundance of elements in the sample (Shackley, 2011). The abundance quantification of the elements is based on the absorption probability of the characteristic x-rays. Assuming a monochromatic and a collimated beam, this probability, is described by Equation 3.1 in accordance with Beer-Lambert law (Schramm, 2000).

$$I_T = I_o \exp\left(-\frac{\mu m}{A}\right) \quad (3.1)$$

where  $I_T$  is the intensity of the transmitted X-rays,  $I_o$ , the is the intensity of the incident X-rays,  $\mu$  is the mass attenuation coefficient,  $m$  is the mass of the sample, and  $A$  the irradiated area. The fluorescent X-rays are generally measured using either of the two types of detection systems: energy dispersive detection (EDXRF) or wavelength dispersive detection (WDXRF).

## 3.2 X-ray Diffraction

X-ray Diffraction uses the Bragg condition to determine the crystal structure of materials. Crystals are made up of a periodic array of atoms that lie within crystallographic planes in regular repeating patterns. When these atoms are struck by x-ray photons, each atom within the planes scatters and emits a secondary x-ray. As a consequence of the wave nature of electrons, the scattered x-rays interfere constructively and destructively to forming diffraction patterns. The constructive diffraction patterns generate angle-dependent intensity distributions that bear information that is unique to the crystal structure of a specific material. The crystal phases are identified by converting the Bragg's peaks to  $d$ -spacing parameters and comparing them against those of standard reference patterns. Since each mineral phase has a set of fingerprints  $d$ -spacings, then its identity is revealed (Le Pevelen, 2016).

### 3.2.1 Bragg's condition

Bragg's condition represents an expression for constructive interference of x-ray diffraction patterns from successive atomic planes of the crystal phases of a material. A monochromatic and collimated beam of X-rays that is incident on the sample under test impinges on it and results in constructive interference whenever the path difference between the incident and the diffracted X-rays is a non-zero integer multiple,  $\eta$  of wavelengths,  $\lambda$ . This is mathematically formulated as shown in equation (3.2) (Pope, 1997).

$$2d_{hkl} \sin \theta = \eta\lambda \quad (3.2)$$

where  $d$  represents the separation distance of the crystallographic planes of the crystal lattice,  $hkl$  represent the miller indices,  $\theta$  represents the angle of incidence formed between the crystallographic plane and the primary x-rays,  $\eta$  is an integer multiple representing the order of diffraction, and  $\lambda$  represent the characteristic wavelength of the primary x-rays. For a cubic unit cell, the relationship between the crystal lattice

parameter  $a$ ,  $d$ -spacing, and the Miller indices ( $hkl$ ) is given Equation 3.3 (Fan, 2012).

$$d = \frac{a}{\sqrt{h^2 + k^2 + l^2}} \quad (3.3)$$

Figure 3.2 illustrates Bragg's condition for constructive X-ray interference.

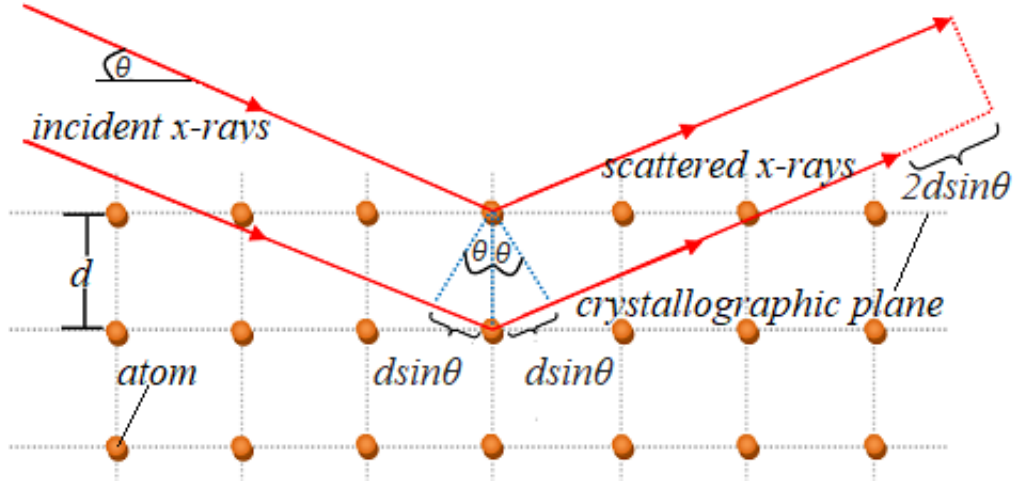


Figure 3.2: Bragg's condition for diffraction in real space. If the condition  $2d_{hkl} \sin \theta = n\lambda$  between the incident and the scattered x-rays is satisfied, then Bragg's peaks occur at respective angles of  $2\theta$  degrees. The  $2\theta$  degrees scanning range of powdered materials optimizes the attainment of lattice diffraction since powders do not assume regular orientation (Le Pevelen, 2016).

XRD spectra are characterized by five fundamental peak parameters namely: peak position, intensity, width, shape, and symmetry (Zhou & Wang, 2003). Each of these parameters has the following physical interpretation: the peak position which is indicated by the angle  $2\theta$  (degrees), and also known as the Bragg's diffraction angle represents the crystal phase in a material. The peak intensity represents the amount of the crystal phase in a material. The peak width represents the size of the crystal in accordance with Scherrer's formulation as shown in equation (3.4) (Valério & Morelhão, 2019).

$$D = \frac{K\lambda}{\beta \cos \theta} \quad (3.4)$$

Where  $D$  is the size of the crystal,  $K$  is a constant of proportionality that is material dependent, the Scherrer constant,  $\beta$  is the line of full width at half maximum (FWHM),  $\lambda$  is the characteristic x-ray wavelength, and  $\theta$  is the Bragg's angle. The shape of an

XRD peak represents the effects that arise from the lattice strain and crystal domain size. The symmetry of the peak represents the effects that arise from aberrations of the Bragg's angle, scattering of reflection plane, and the geometrical orientation of the sample relative to the instrument.

Ideally, each of the XRD peaks would have been observed as an infinitely-sharp delta-function if every single crystal assumed a perfect orientation with the instrumentation but practically, the peaks appear somewhat broadened into intensity distributions centered on  $2\theta$  degrees. This is a consequence of imperfections such as beam divergence and crystal dynamics such as lattice vibrations, thermal fluctuations, crystal strain, and stress.

### **3.2.2 X-ray Diffraction of Cementitious Materials**

The raw materials of cement are made up of different crystal phases, namely: calcium carbonate ( $\text{CaCO}_3$ ), quartz ( $\text{SiO}_2$ ), siderite ( $\text{FeCO}_3$ ), bauxite ( $\text{Al}_2\text{O}_3$ ), and gypsum ( $\text{CaSO}_4$ ). The mineralogical phases of limestone, the chief raw material of cement, varies according to its purity level. The mineralogical phases of high purity limestone mainly consist of  $\text{CaCO}_3$  polymorphs (calcite, aragonite, and vaterite), and chemical mixtures of Fe, Mn, Mg, Al, Si, and C (Dukic et al., 2018). Low purity limestone (kunkur) mainly consists of dolomite ( $\text{CaMg}[\text{CO}_3]_2$ ), ankerite ( $\text{Ca}(\text{Fe}, \text{Mg})[\text{CO}_3]_2$ ) and other impure forms of calcium carbonate-based compounds. The typical crystal phases of limestone (99.2% purity) are represented in Figure 3.3.

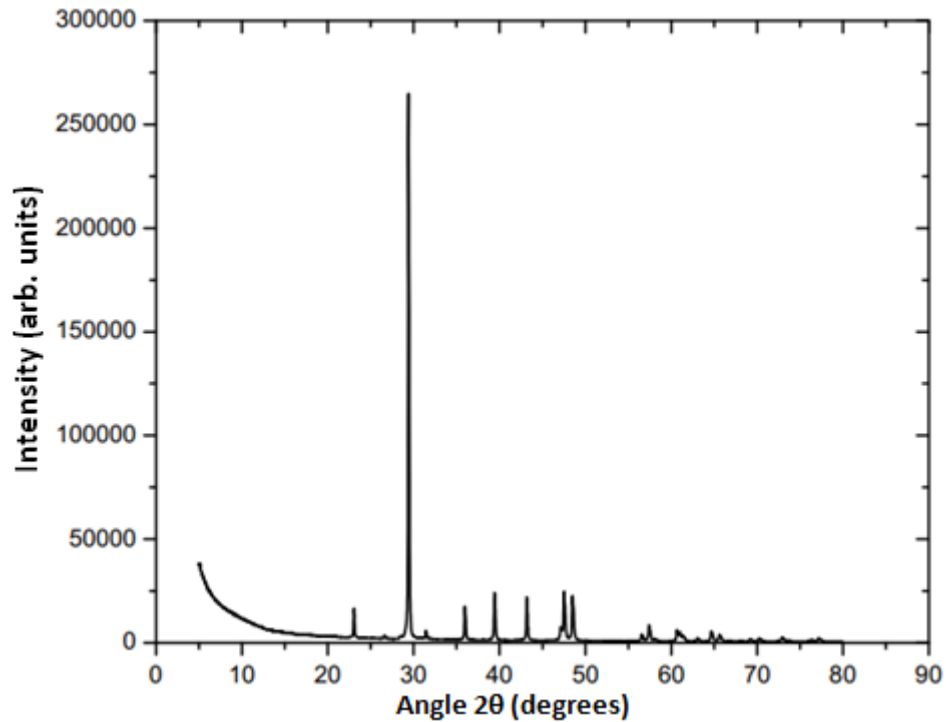


Figure 3.3: XRD peaks representing the crystal phases of 99.2% pure limestone (Šiler et al., 2018).

High purity limestone is distinguished from dolomite by Bragg's reflection (104) which corresponds to  $2\theta=30^\circ$ . Shifting of this reflection is ascribed to the presence of other mineral phases (the impurities).

### 3.3 Raman Scattering

The Raman scattering uses characteristic vibration bands that are unique to every phase in a material, thus it can distinguish polymorphic crystal phases (Behrens et al., 2006). The characteristic vibration bands are identified based on inelastic scattering of light (Raman scattering) by the molecules in a material. The vibration mechanisms of these molecules can be described from the perspectives of classical and quantum physics.

#### 3.3.1 Classical Description of Raman Scattering

In the perspective of classical physics, the vibration of molecules in materials can be modelled in Hooke's formalism, where the atoms behave like point masses connected by chemical bonds which represent a weightless elastic cord (Sjögren, 2018), as illus-

trated in Figure 3.4.

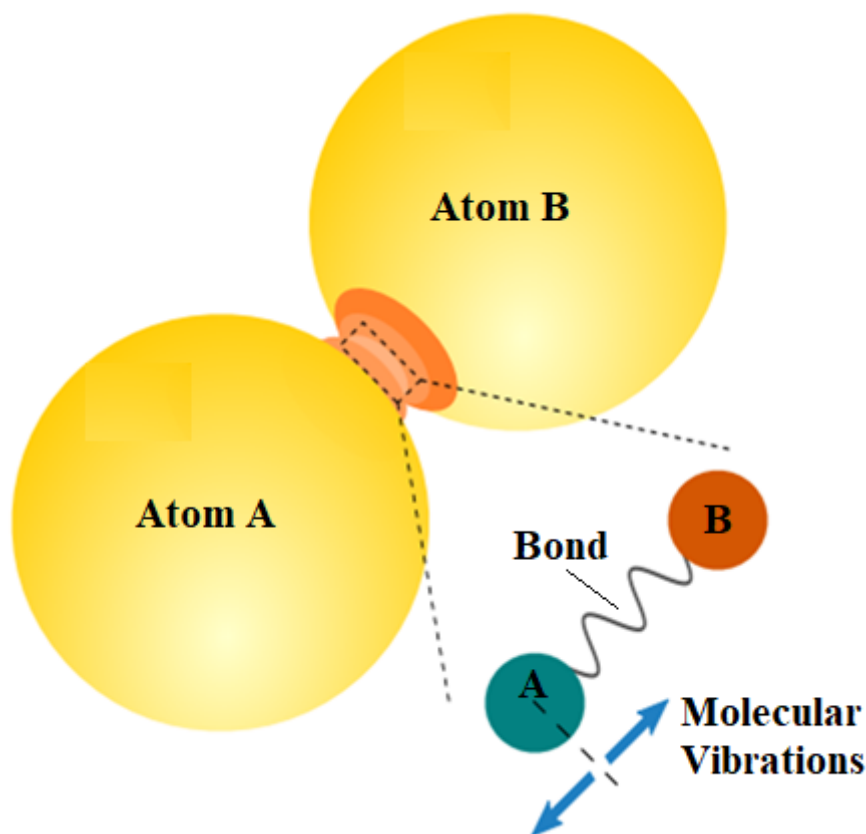


Figure 3.4: Classical illustration of molecular vibrations in a diatomic Molecule (Schmidt et al., 2016).

According to Hooke's law, the approximate vibration frequency of the bond is given by Equation 3.5 (Siebert & Hildebrandt, 2008).

$$\nu = \frac{1}{2\pi c} \sqrt{\frac{k}{m}} \quad (3.5)$$

Where:  $\nu$  is the fundamental vibration frequency in wavenumber ( $\text{cm}^{-1}$ ),  $c$  is the speed of light,  $k$  is the bond force constant, and  $m$  is the atoms reduced mass. The Raman-active vibrations are enabled by a net change (non-zero) in the first derivative polarizability,  $\alpha$  of molecular vibrations with respect to the normal coordinate,  $q$  of vibration according to Equations 3.6 and 3.7 respectively (Leng, 2013).

$$\left(\frac{d\alpha}{dq}\right)_{q=0} \neq 0 \quad (3.6)$$



Where:

$$\alpha = \frac{\mu}{E} \quad (3.7)$$

Where:  $\mu$  is induced dipole moment of a molecule which scatters the incident light;  $E$  is the external electric field that induces the molecule polarizability.

Fundamentally,  $\alpha$  signifies the ability to distort a molecule. The polarizability ( $\alpha$ ) depends on the coordinates of the atoms in the molecule, which varies with the time,  $t$  at the molecular vibrational frequency,  $\omega$  as shown in Equation 3.8 (Wabwile, 2018).

$$\alpha(E) = \alpha E_o \cos(\omega t) \quad (3.8)$$

However, molecular polarizability changes with bond lengths and are restricted to discrete vibrational energies, which have been elaborated by the quantum picture in the ensuing section.

### 3.3.2 Quantum Description of Raman Scattering

The quantum description of Raman scattering is pictured by the electronic transitions of molecular different vibrational energy levels that comprise of a Rayleigh spectrum, Stokes shifted spectra, and anti-Stokes shifted spectra (Mikla & Mikla, 2014). The scattering event obeys the law of conservation of total momentum and energy as given by Equation 3.9 respectively (Meyer, 2015).

$$\begin{aligned} \mathbf{k}_s - \mathbf{k}_i &= \pm \mathbf{K} \\ \omega_s - \omega_i &= \pm \omega(\mathbf{K}), \end{aligned} \quad (3.9)$$

where  $\mathbf{k}_s$  and  $\omega_s$  is the wavevector and frequency of the scattered photon. In Equations 3.9, the plus and minus signs correspond to the anti-Stokes and Stokes scattering respectively. When a molecule absorbs a photon, the former is excited to imaginary states and leads to Raman or Rayleigh scattering upon re-emission. In both cases, the final state has the same electronic energy as the initial state but higher in vibrational

energy for Stokes Raman scattering, the same for Rayleigh scattering, and lower for anti-Stokes Raman scattering as illustrated in Figure 3.5.

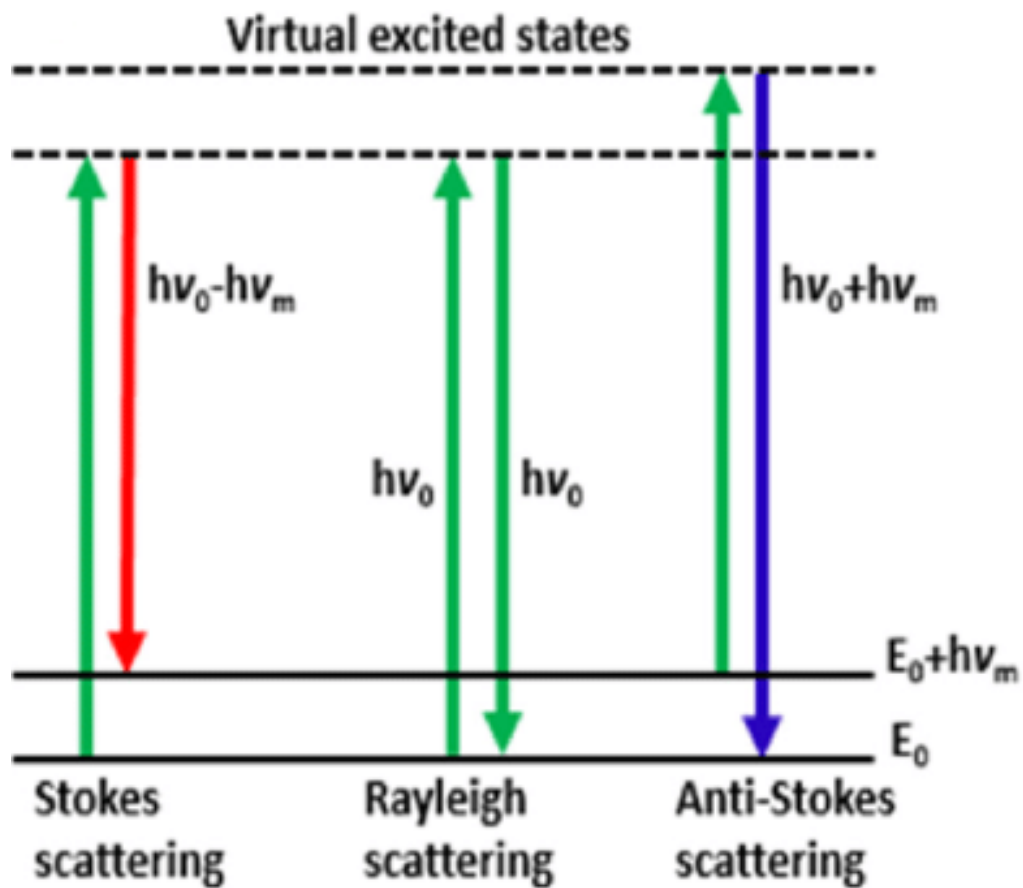


Figure 3.5: Vibrational excitations in Raman scattering (Lohumi et al., 2017).

A typical Raman spectra consists of the Stokes and anti-Stokes spectra symmetrically shifted from the Rayleigh spectrum. This symmetrical frequency shift is a consequence of a gain or loss of a vibrational quantum of energy in either case. The Stokes shifted spectra are typically more intense than anti-Stokes shifted as illustrated in Figure 3.6.

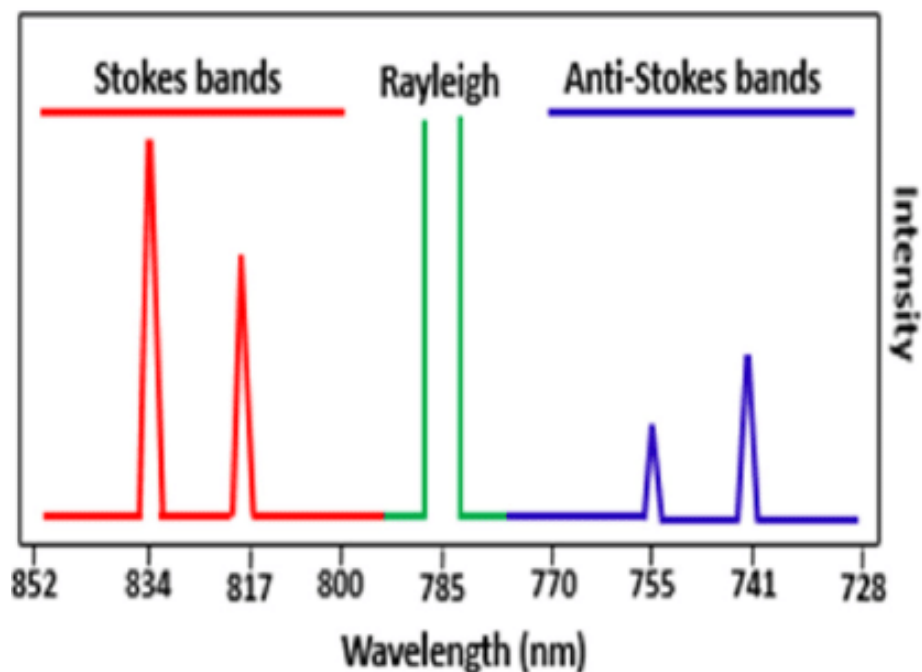


Figure 3.6: Typical spectra of Raman scattering (Lohumi et al., 2017).

The frequency of the Raman shifted photons is dependent upon the vibrational state of the molecule under study. The knowledge of these vibrational frequencies makes Raman spectroscopy a powerful technique for studying the structure of molecules.

### 3.3.3 Raman Scattering of Calcite-based Materials

Due to the difference in crystal structures, the carbonate mineralogical phases in these materials can be readily distinguished based on the molecules' internal vibration modes. These vibrational modes include  $\nu_1$ ,  $\nu_2$ ,  $\nu_3$ , and  $\nu_4$ , and they respectively arise from symmetric/anti-symmetric stretching, and in-plane/out-of-plane bending of the calcium carbonate molecules (Behrens et al., 2006). These vibrational modes are illustrated in Figure 3.7.

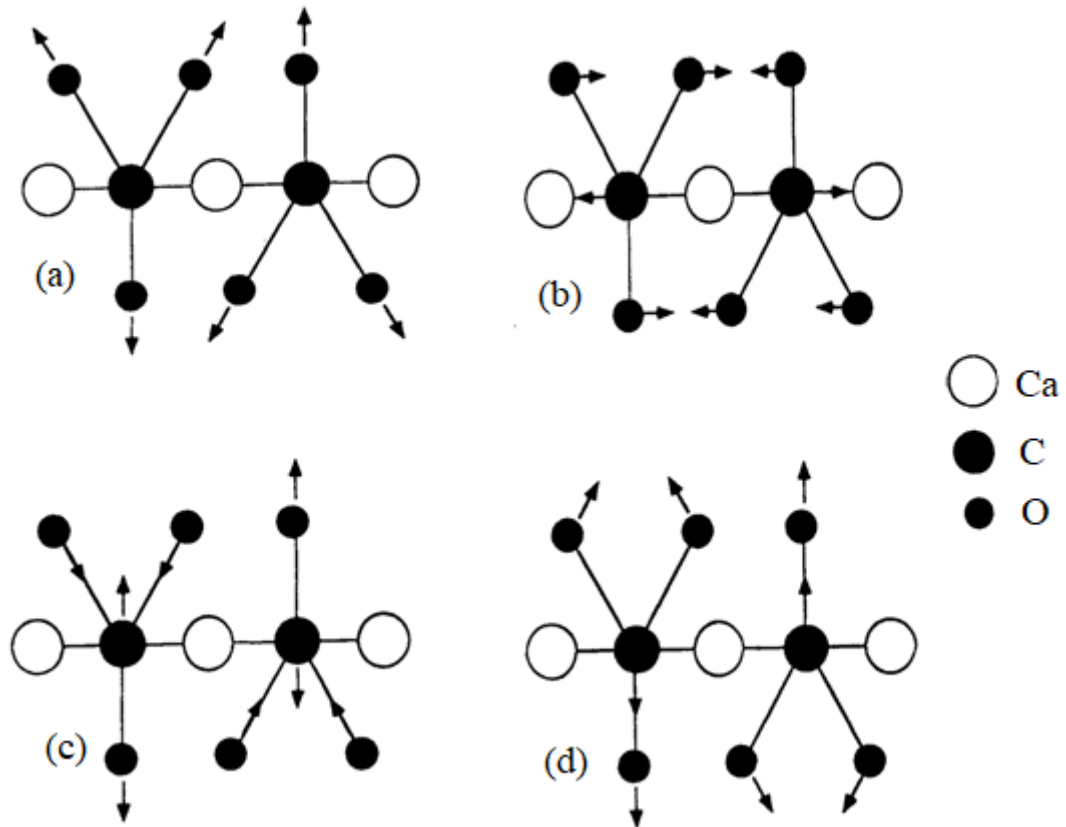


Figure 3.7: Schematic illustration of the four vibrational modes of  $\text{CO}_3^{2-}$  in of calcium carbonate. (a) represent  $\nu_1$  - the symmetric stretching, (b) represent  $\nu_2$  - the anti-symmetric stretching, (c), represent  $\nu_3$  - the in-plane bending, and (d) represent  $\nu_4$  - the out-of-plane bending (Behrens et al., 2006).

### 3.4 Raw Mix Moduli

In cement, raw mix moduli refer to the relations between the oxides of cement and it is represented by a group of five moduli. These are the Hydraulic Modulus (HM), lime Saturation Factor (LSF), Silica Ratio (SR), Alumina Ratio (AR), and the Sulfatisation Modulus (SM) and are given by Equations 3.10 – 3.15 (Paine, 2019).

#### 3.4.1 Hydraulic Modulus (HM)

The hydraulic modulus (HM) is expressed as:

$$HM = \frac{\text{CaO}}{\text{SiO}_2 + \text{Al}_2\text{O}_3 + \text{Fe}_2\text{O}_3} \quad (3.10)$$

HM indicates the energy intensiveness of clinkerizing the raw mix. The hydraulic modulus is limited to  $1.7 \leq HM \leq 2.3$  (Aldieb & Ibrahim, 2010). HM is also an indicator of the hydraulic activity that enhances strength development.

### 3.4.2 Lime Saturation Factor (LSF)

The lime saturation factor (LSF) is expressed as:

$$LSF = \frac{CaO + (0.75)MgO}{(2.80)SiO_2 + (1.20)Al_2O_3 + (0.65)Fe_2O_3} \quad (3.11)$$

However, if the value is higher than 2 wt.%, Equation 2.2 is rendered inappropriate for the determination of LSF. This is because excess MgO tends to be present as free periclase mineral after calcination, thus giving the incorrect values of LSF (Paine, 2019). The British Standard -12, provides an alternative formula for determining the LSF of clinker materials containing than 2 wt.% MgO, as given by Equation 2.3 (Winter, 2005).

$$LSF = \frac{CaO - (0.7)SO_3}{(2.80)SiO_2 + (1.20)Al_2O_3 + (0.65)Fe_2O_3} \quad (3.12)$$

The LSF is used to determines the potential relative proportions of alite to belite phases in the clinker. The lime saturation factor of the raw mix is limited to  $0.80 \leq LSF \leq 0.95$  (Aldieb & Ibrahim, 2010). The LSF is also an indicator of excess free lime in the clinker. In principle, the LSF value equivalent to 1.0, indicates that the free lime is completely combined with belite to form alite, and therefore,  $LSF > 1.0$  indicates excess free lime (Aldieb & Ibrahim, 2010). The excess free lime hampers the burnability of the raw mix (Aldieb & Ibrahim, 2010).

### 3.4.3 Silica Ratio (SR)

The silica ratio (SR), also known as the silica modulus, is expressed as:

$$SR = \frac{SiO_2}{Al_2O_3 + Fe_2O_3} \quad (3.13)$$

The silica modulus influences the burning process of the raw mix. The silica modulus of the raw mix is limited to  $1.5 \leq SR \leq 3.2$  (Aldieb & Ibrahim, 2010). This implies that the proportion of silica should be higher than that of the weighted sum of alumina and ferrite. High SR indicates more calcium silicates in the clinker and less aluminate and ferrite. High SR clinker is indicated by the formation of ring-like coatings in the kiln. The coatings are due to the distinct burning zones of the raw mix that are attributed to poor burnability of the raw mix (Aldieb & Ibrahim, 2010).

#### 3.4.4 Alumina Ratio (AR)

The alumina ratio (AR) is expressed as:

$$SR = \frac{Al_2O_3}{Fe_2O_3} \quad (3.14)$$

It is an indicator of the possible relative amounts of aluminate and ferrite phase in the clinker. The alumina modulus of the raw mix is limited to  $1.5 \leq AR \leq 2.0$  (Aldieb & Ibrahim, 2010). This range implies that the clinker should have more aluminate than ferrite phases. A combination of high AR and low SR is attributed to quick setting of the resultant cement.

#### 3.4.5 Sulfatisation Modulus (SM)

The sulphate modulus (SM), also known as the sulfatisation of the alkali, is expressed as:

$$SM = \frac{SO_3}{(1.292)Na_2O + (0.850)K_2O} \quad (3.15)$$

SM determines the molar balance between sulphur and alkalis in the raw mix. It indicates the probability of sulphur or alkali accumulations in the kiln. In principle, the SM at 1.0, indicates complete combination of the alkalis with  $SO_3$ , and thus the formation of alkali sulphates. The SM of the raw mix is limited to  $0.8 \leq SM \leq 1.2$ . The magnitudes of SM less than 0.8 indicate excess alkalis, which lead to formation of alkali rings in the kiln. On the other hand, magnitudes of SM higher than 1.2 indicate excess sulphur,

which lead to formation of a solid solution with the  $C_2S$  phase. This inhibits the formation  $C_3S$  phase. As a result, the  $C_2S$  phase is enriched at the expense of  $C_3S$  phase, thus reducing the clinker quality (Winter, 2005).

### 3.5 Theory of Blaine Permeability

Powders play an important role in the manufacture of cement, for instance, size variation, shape, and surface roughness of their particles affect their functional behaviour. Blaine permeability method for testing particle fineness takes care of these characteristics, unlike the laser diffraction techniques that assume spherical shape for all particles. The permeability calculations are governed by Darcy's principle (Singh & Cai, 2019), which states that the rate of flow is directly proportional to the pressure gradient causing flow. Permeability measurements of cementitious materials require a relation of specific surface area and the unit mass. The specific surface area (SSA) according to the permeability method is evaluated using Equation 3.16, which is the Kozeny-Carman equation for granular beds (Kruczek, 2014; Niesel, 1973).

$$SSA = \frac{14}{\rho(1 - \epsilon)} \sqrt{\frac{\epsilon^3 A \Delta p}{\eta l \Phi_v}} \quad (3.16)$$

where factor 14 is an empirical constant,  $\rho$  is the density of the powder,  $\epsilon$  is the porosity of the powder,  $A$  is the permeated area,  $\Delta p$  is the pressure difference,  $\eta$  is the kinematic viscosity of the permeating medium (Stokes),  $l$  is the height of the powder bed, and  $\Phi_v$  is the flow rate. The application of Equation 3.16 in the Blaine technique reduces to Equation 3.17.

$$SSA = \frac{C}{\rho(1 - \epsilon)} \sqrt{\frac{\epsilon^3 t}{\eta}} \quad (3.17)$$

where  $C$  is a constant of the Blaine apparatus, and  $t$  is the running time between the indicated levels of the Blaine apparatus. The Blaine method for determination of SSA of materials is a comparative criterion that employs Equation 3.17 to determine the SSA of one material (known as the standard or reference) and then uses time is the only

variable to determine the SSA of another material (sample under test) in accordance to Equation 3.18 (ASTM C204-07, 2007).

$$S = S_s \sqrt{\frac{t}{t_s}} \quad (3.18)$$

where  $S$  is the specific surface area of the sample,  $S_s$  is the specific surface area of the standard,  $t$  is the flow time of the sample material, and  $t_s$  is the flow time of the standard. This technique, being comparative rather than absolute requires calibration of the Blaine apparatus after every test in order to obtain accurate results.



## CHAPTER 4

### MATERIALS AND METHODS

#### 4.0 Introduction

This chapter describes the sample preparation and characterization techniques that were used in this study. The sample preparation steps involved but not limited to cleaning, drying, and crushing the rock, pulverization, ball milling, and pelletization. The characterization techniques employed were Energy Dispersive X-ray Fluorescence (T NEX-CG “Rigaku”) - Physics Department, University of Nairobi; Wavelength Dispersive X-ray Fluorescence (PANalytical AXIOS) - Physical Testing Laboratory, East African Portland Cement Ltd., Athi River; X-ray Diffractometry (Bruker D8 Discover) - Microscopy and Microanalysis Unit, University of the Witwatersrand; Raman spectroscopy - Laser Lab, Physics Department, University of Nairobi; Scanning Electron Microscopy - School of Physics, University of Pretoria; Micro-sieve and Blaine analyses - Physical Testing Laboratory, East African Portland Cement Ltd., Athi River. These equipments were used to study the chemical composition, mineralogy, morphology, particle size distribution, and specific surface area of Matisaa gray rock. The characteristics of this material were compared against Konza kunkur which is an established raw material of cement utilized by East African Portland Cement Company Ltd. (EAPCC), Athi River, Kenya, as the chief source of calcium oxide.

#### 4.1 Sample Preparation

The original sample of Matisaa gray rock was in the form of a stone and its conversion into powder form (compressed and uncompressed) involved several steps, which were guided by the flow diagram shown in Figure 4.1.

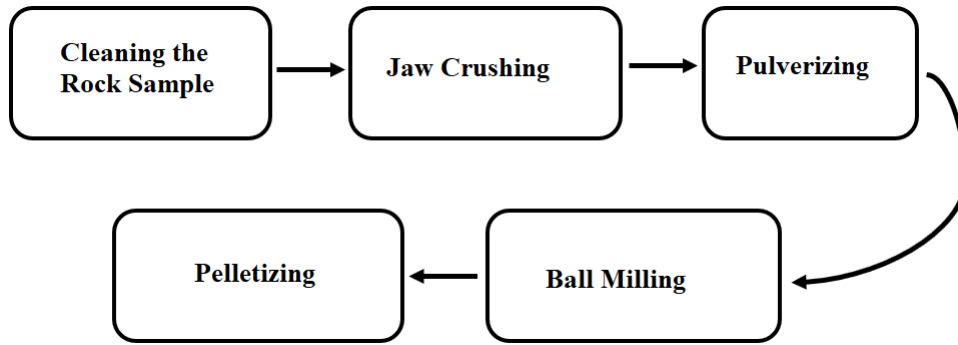


Figure 4.1: Flow diagram showing the steps that guided the conversion of Matisaa gray rock into powder.

Foremost, Matisaa gray rock was cleaned in a sonicator for 30 minutes at room temperature to remove any surface contaminants and dried in an oven at  $105^{\circ}\text{C}$  for 24 hours to attain a constant dry weight. It was then crushed into sizes of 10 – 20 mm using a laboratory jaw crusher. This was done to reduce the rock into sizes that could be pulverized by a Herzog pulverizing machine. After pulverization, the sample was ground using a ball mill for 30 minutes to produce average grain sizes of the micron size. To ensure that the grain size was of micron range the sample was passed through a 1000  $\mu\text{m}$ -mesh sieve. Only the particles that passed through the 1000  $\mu\text{m}$ -mesh sieve were considered for subsequent experiments.

The sample was further divided into two portions; one for uncompressed powder tests and the other one for compressed powder tests. The sample was mixed with 10% wax (binder) in a 22 mm aluminum cup and hydraulically pressed at a constant force of 10 kN to produce 2 mm-thick and 22 mm-wide disc-shaped pellets. The compression force was maintained for 60 seconds to ensure the surface consistency and mechanical integrity of the pellets that were tested under vacuum conditions. The steps that were followed to prepare the sample for chemical analyses are summarized in Figure 4.2.



Figure 4.2: Schematic representation of the sample preparation steps: (a) As-collected sample, (b) Cleaned rock, (c) Crushed to sizes of 10 – 20 mm, (d) Pulverizing to the size of  $< 1000 \mu\text{m}$ , (e) Sifted dust of micron-size particles, (f) Pelletizing to the size of 5 mm-thick and 22 mm-wide discs

## 4.2 Characterization Techniques

The samples were studied for chemical composition, crystal structure (mineralogy), morphology, particle size, and specific surface area. These are the basic parameters that determine the quality of cementitious materials (Lothenbach et al., 2011). The chemical composition was studied using the X-ray fluorescence technique (EDXRF and WDXRF). The crystal structure was studied using the X-ray diffraction technique (XRD) and light scattering techniques (Raman spectroscopy). The grain morphology was studied using scanning electron microscopy (FESEM microscope types), whereas, the particle size distribution was studied using the micro-sieving technique ( $45 \mu\text{m}$  and  $90 \mu\text{m}$ -mesh sieves). The specific area was studied using an air permeability technique (Blaine Apparatus).

### 4.2.1 Chemical Composition

The chemical composition of the samples was studied using the X-ray Fluorescence technique (XRF). This study was carried out to establish the proportions of the individual cement elements and that of the corresponding oxide in Matisaa gray rock. The individual cement elements were studied using the EDXRF instrument shown in Figure 4.3.

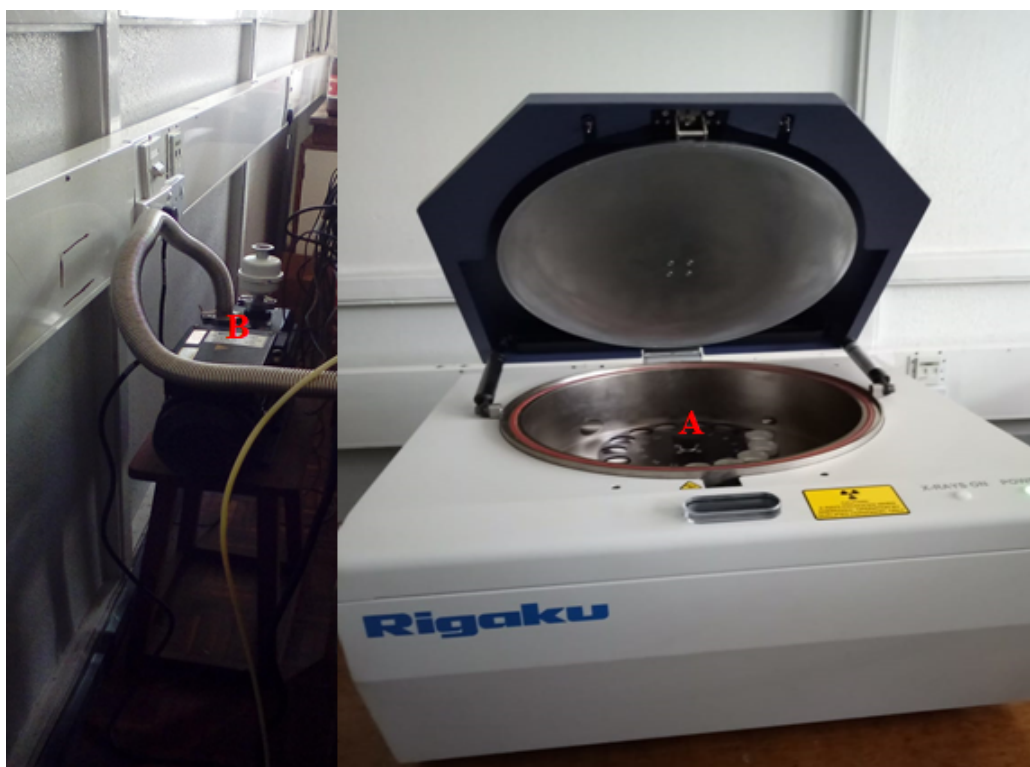


Figure 4.3: A photograph of the EDXRF instrument (T NEX-CG “Rigaku”) that was used in this work. (Courtesy of the University of Nairobi, Kenya). The parts labelled A - shows the sample irradiation chamber, and B - vacuum pump.

This equipment has 15 autosampler units in the X-ray irradiation chamber. The sample was run in compressed form in a vacuum atmosphere. The software that runs this instrument is programmed to quantify the elemental abundance in parts-per-million (ppm). On the other hand, the cement oxides that constitute Matisaa gray rock were studied using the WDXRF instrument shown in Figure 4.4. This equipment runs on software that quantifies the composition abundance in percentage weight (wt.%).



Figure 4.4: A photograph of the WDXRF instrument (PANalytical AXIOS) that was used in this work. (Courtesy of East African Portland Cement Ltd., Athi River, Kenya). The parts labelled A - shows the sample chamber, and B - the display.

## 4.2.2 Crystal Phase Composition

To examine the crystal phases in Matisaa gray rock, the samples were characterized using the X-ray diffractometer shown in Figure 4.5. This characterization was done on uncompressed powders since it enhances the optimization of diffraction and therefore improved identification of the crystalline phases.

A parallel test of the mineral phases in Matisaa gray rock sample was run in parallel with that of Konza kunkur. The samples were mounted the sample stage and the instrument was set to operate at 8.0 kV Cu- $K_{\alpha}$  radiation ( $\lambda = 1.5418 \text{ \AA}$ ), 40 kV and 40 mA at  $2\theta$  Bragg angle range of  $10^{\circ}$  to  $90.0062^{\circ}$  using a step size of  $0.0264^{\circ}$ . The setting of the operating parameters was enabled by *DiffraC.suite* software, which is the program that runs the entire instrument.

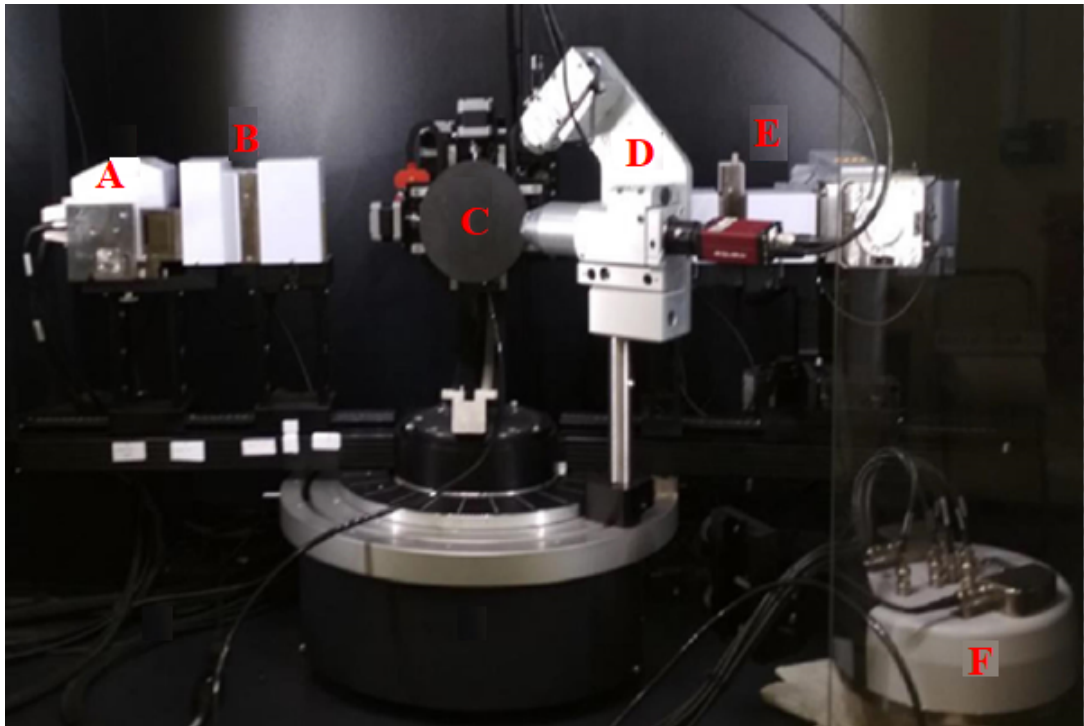


Figure 4.5: A photograph of the XRD equipment (Bruker D8 Discover) used in this work (Courtesy of University of the Witwatersrand, South Africa). The parts labelled A - shows the detector, B - the secondary optics, C - the sample stage, D - the copper X-ray tube, E - the primary optics, and F - the vacuum pump system.

The XRD data obtained were analyzed using *EVA* program, which is a computer code for identifying crystal phases of materials and the respective phase composition. This program compares the diffraction pattern of the sample against a database containing reference patterns.

Even though the XRD technique is the most ideal technique for structural analysis of crystals, its efficiency is however limited by the weak diffraction of low *Z* elements. Additionally, the XRD may sometimes not detect crystals with minute elemental concentrations. In the present study, where the sample under investigation was suspected to contain low *Z* elements, a complementary technique that can furnish this information was necessary. The Raman spectroscopy was thus chosen. The Raman spectrometer set-up that was used to study the vibrational modes of the crystals in Matisaa gray rock is shown in Figure 4.6.

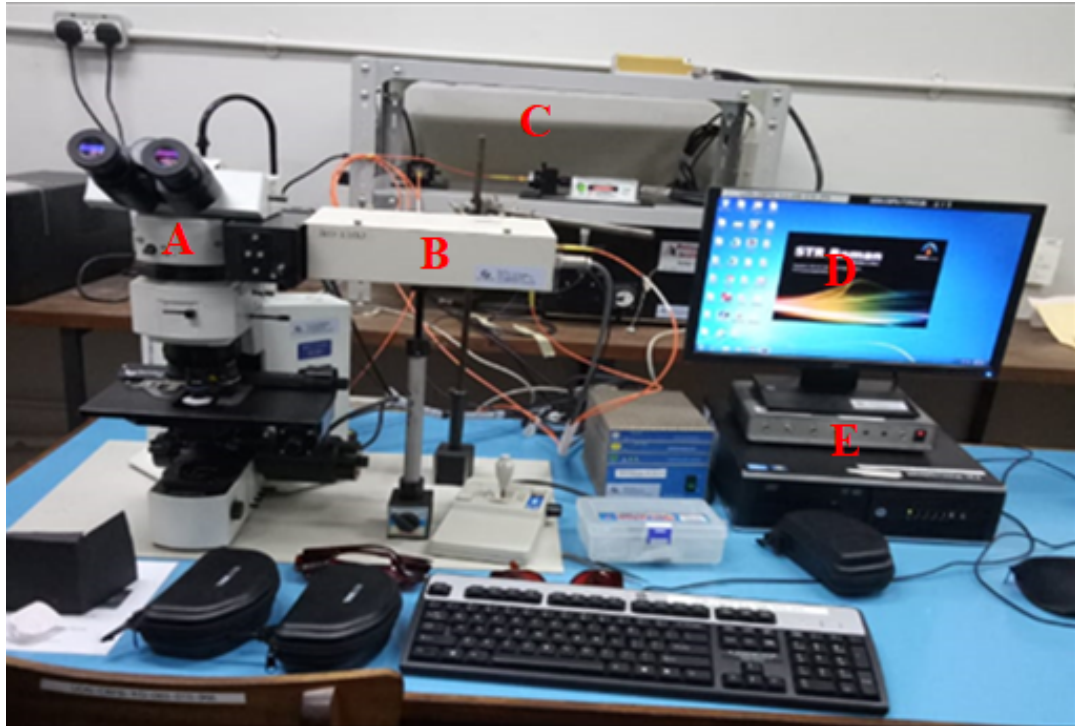


Figure 4.6: A photograph of the Raman spectrometer that was used in this work. (Courtesy of the University of Nairobi, Kenya). The parts labelled A - shows the microscopy unit, and B - the light filtration unit, C - the laser unit, D - the display, and E-the central processing unit.

The measuring system was first calibrated against the  $520.5\text{ cm}^{-1}$  spectrum of a silicon wafer at  $18\text{ }^{\circ}\text{C}$ . The sample was placed and aligned on the stage controller, which was interfaced with a Raman microscope system. The Raman microscope system includes the monochromator, light filtration system, and detector CCD camera. The spectra were excited by a  $532\text{ nm}$  He – Ne laser at a resolution of  $2.0\text{ cm}^{-1}$  in the frequency range of  $50 - 4000\text{ cm}^{-1}$ . The spectral acquisition was done using *STR* Raman spectrometer software (Seki Technotron Corporation, Japan). The spectral acquisition was repeated three times in three different regions of the sample.

The Raman spectra of Matisaa gray rock were obtained by filtering the background radiation due to Raman fluorescence using the *Vancouver Raman Algorithm* software package. This program extracts Raman signals from the measured data that usually has Raman signals due to the sample and background fluorescence signals. The Raman signatures of the sample were identified using the ‘search-match’ routine.

### 4.2.3 Morphological Studies

The surface morphology of Matisaa gray rock was probed using a FESEM instrument.

A FESEM setup with its main instrumental parts is shown in Figure 4.7.

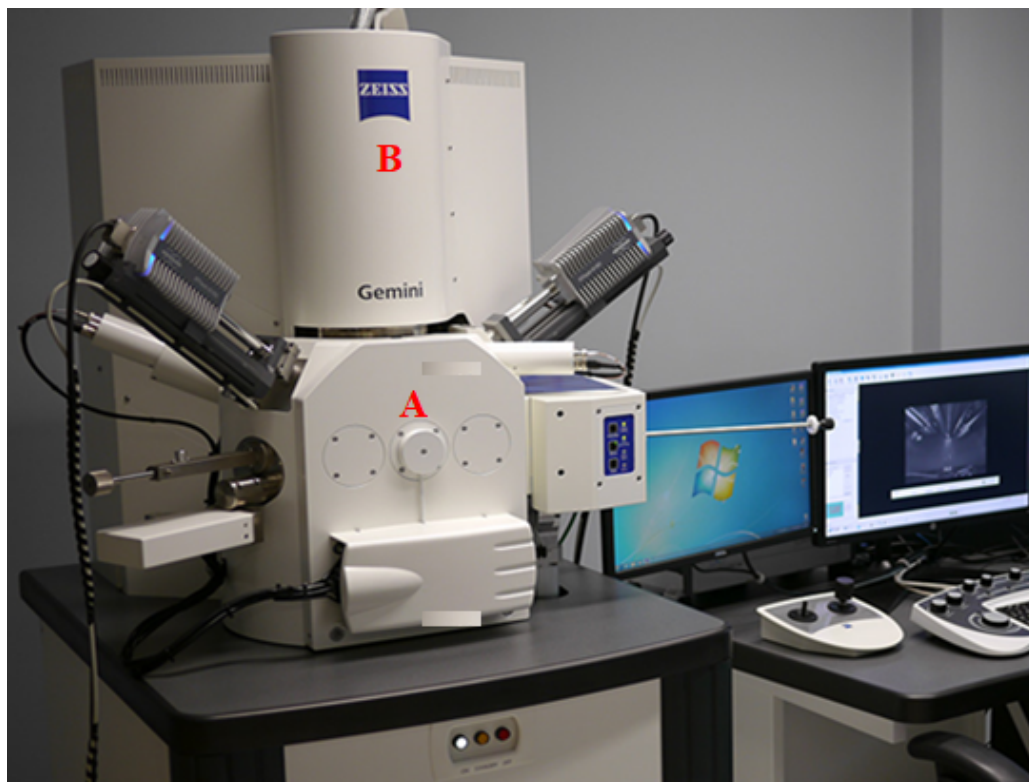


Figure 4.7: A photograph of the SEM equipment (Zeiss ULTRA Plus) that was used in this work. (Courtesy of the University of Pretoria, South Africa). The parts labelled A - shows the vacuum-pumped chamber, and B - the Gemini column hosting the beam focusing optics.

The rock powder was mounted onto the stubs of the FESEM instrument located in the vacuum-pumped chamber and the electrons emitted from the electron gun were accelerated to the sample at a voltage of 15 kV and a working distance of 12.5 mm. The electron beam was focused by an optical set in the Gemini column. Scanning of the sample surface was carried with an aid of *SmartSEM* software which the entire instrument runs on. The sample was insulating to the electron beam and was therefore unmounted and sputter coated with two layers (10 nm) of gold-palladium coating before further scanning. A thin layer of gold and palladium inhibits electrostatic charging and thus enhancement of optical reflectivity (Mohammed et al., 2013). The sample was then remounted for FESEM scanning.



#### **4.2.4 Particle Size Distribution**

The particle size distribution for milled samples was carried out on 90  $\mu\text{m}$  and 45  $\mu\text{m}$ -sieve, respectively to obtain two samples, one of  $< 90 \mu\text{m}$  other of  $< 45 \mu\text{m}$  by following the ASTM C618 – 12a, (2012) method. For  $< 90 \mu\text{m}$  particle size evaluation, 50.000 g of the sifted MGR dust were put into a 90  $\mu\text{m}$ -sieve and gradually agitated to freely pass through the sieve mesh. The mass of the particles that passed was recorded and further sieved through the 45  $\mu\text{m}$ -sieve. Due to the fineness level of particles  $< 45 \mu\text{m}$ , wet sieve evaluation was carried out for the  $< 45 \mu\text{m}$ , where the complete passage of the sample was aided by applying a controlled stream of distilled water over the sieve. The wet mass of the sample was recorded and dried in an oven at 105 °C for 24 hours to attain a constant mass. The constant mass was recorded as the new mass of the sample. A similar parallel procedure was applied to Konza kunkur.

#### **4.2.5 Specific Surface Area Analysis**

The specific surface area (SSA) of Matisaa gray rock was measured according to the ASTM C204-07, (2007) standard test method for determining the specific surface area of hydraulic cements by air permeability. Matisaa gray rock sample was run and compared to that Konza kunkur in the Blaine Analyzer.

The Blaine test was carried out by loading the samples (uncompressed powders) in the sample compartment. The samples were tightly mounted on the top of a U-tubed manometer which was filled partially with dibutyl phthalate (Blaine fluid). The time taken for the dibutyl phthalate to drop to a given position of the manometer column was measured. The procedure was repeated two more times for validation of the results consistency. The measured time was then used to compute the specific surface area of the sample in accordance with Equation 3.18. The Blaine apparatus that was used to carry out the SSA of the samples are shown in Figure 4.8.



Figure 4.8: A photograph of the Blaine Analyzer (CM/L 0278348) that was used in this work. (Courtesy of East African Portland Cement Ltd., Athi River, Kenya). The parts labelled A - shows the sample compartment, B - the U-manometer, C - rubber bulb.

## **CHAPTER 5**

### **DATA PRESENTATION, ANALYSIS, AND DISCUSSIONS**

#### **5.0 Introduction**

In this chapter, the experimental findings, analyses of the data obtained that characterizes Matisaa gray rock, and discussions of the results are presented. The experimental results include the measured concentration of individual elements and oxides of cement, phase composition, particle size, and specific surface area.

#### **5.1 Chemical composition**

The elements found in cement were also found in Matisaa gray rock in the following concentration levels: 294, 000 ppm for Ca, 45, 200 ppm for Si, 16, 700 ppm for Al, 3, 940 for Fe, 3, 290 for K, and 164 ppm for S.

Graphically, the concentration of these elements in Matisaa gray rock is shown in Figure 4.1.

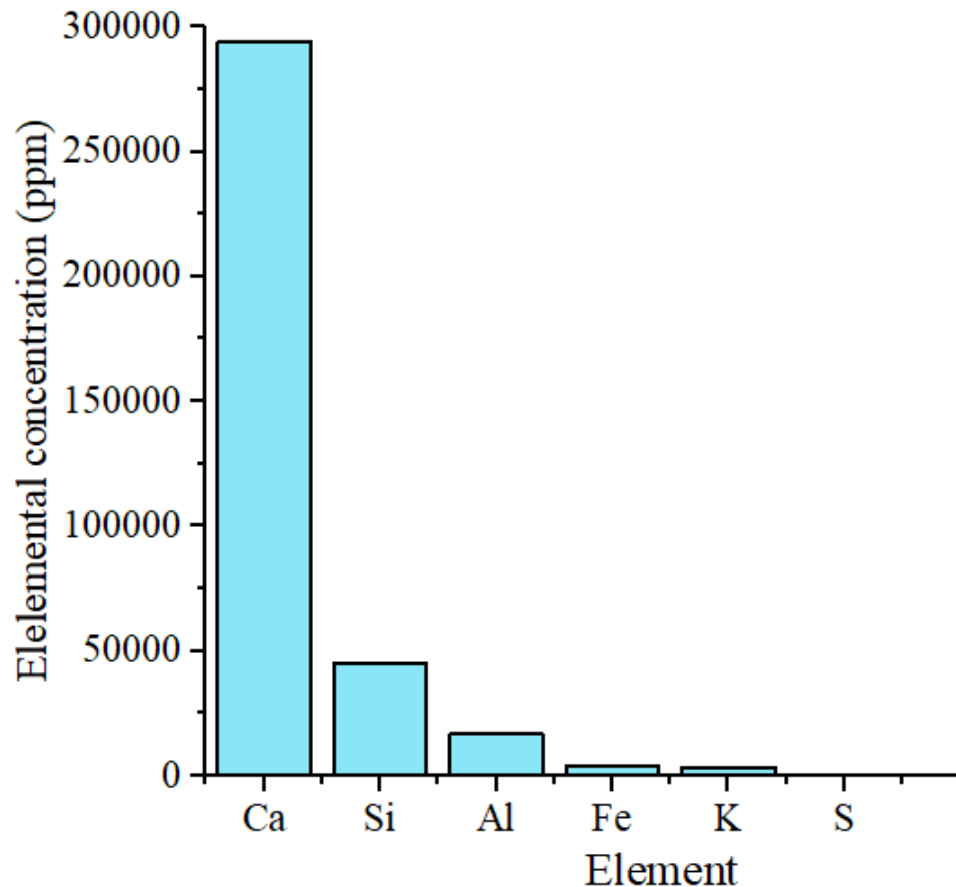


Figure 5.1: A bar graph showing the comparison of the elemental composition of Matisaa gray rock.

Ca, the marker of cement, as defined by Obiajunwa et al., (2000), has the highest concentration level (Figure 5.1). The major elements in limestone are Ca, Si, Al, Fe, K, and S (Obiajunwa & Nwachukwu, 2000). The concentration levels in parts per million (ppm) of the major elements in a standard limestone should be 562, 100 ppm for Ca; 272 850 ppm for Si; 60, 290 ppm for Al; 11, 416 ppm for Fe; 27, 624 ppm for K; and null for S (Akpan et al., 2011). The oxide composition of Matisaa gray rock in comparison with Kunkur is shown Table 5.1.

Table 5.1: Cement oxides (wt.%) in Matisaa gray rock and Konza kunkur

Oxide	Matisaa gray rock	Konza kunkur
CaO	39.03 – 46.42	34.43 – 47.46
SiO <sub>2</sub>	13.92 – 16.79	14.93 – 17.13
Al <sub>2</sub> O <sub>3</sub>	0.47 – 4.81	2.93 – 4.98
Fe <sub>2</sub> O <sub>3</sub>	0.55 – 1.04	0.66 – 2.24
MgO	1.56 – 3.56	1.49 – 3.35
SO <sub>3</sub>	3.30 – 6.06	-
K <sub>2</sub> O	0.59 – 2.64	-
Na <sub>2</sub> O	0.11 – 0.21	-

From the Table 5.1, it is observed that Matisaa gray rock contains the fundamental oxides suitable for the manufacture of cement. A graphical comparison of the major fundamental oxides of cement in Matisaa gray rock against Konza kunkur is depicted in Figure 5.2.

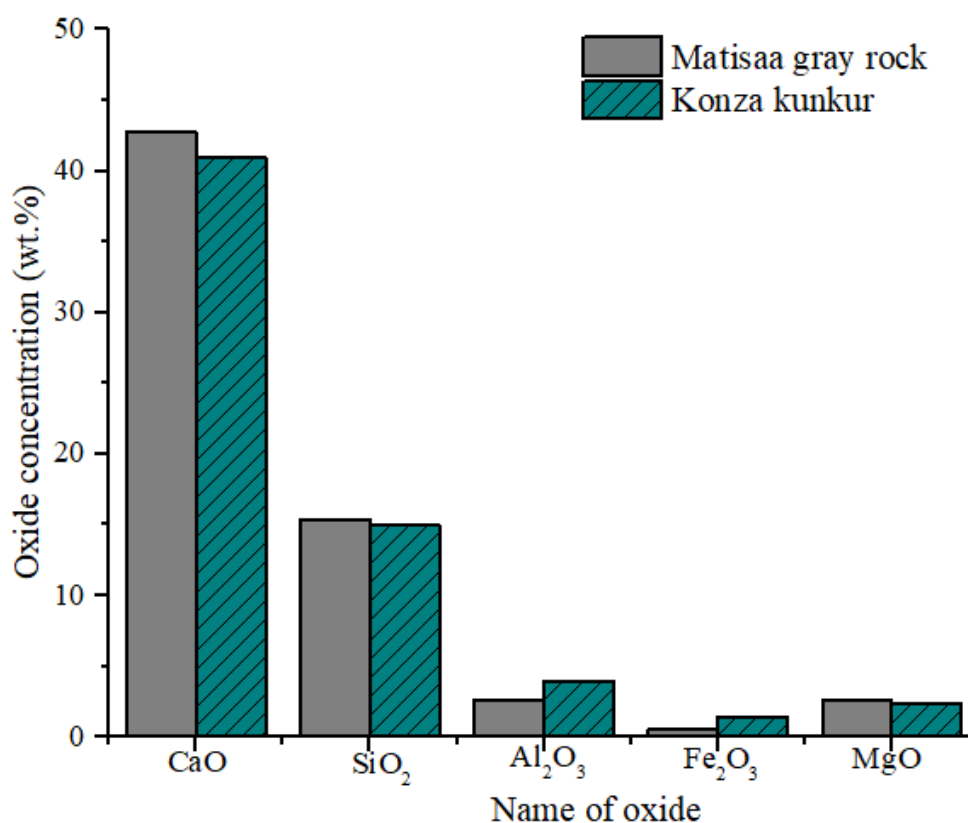


Figure 5.2: Comparative bar graph of the average concentration of the main cement oxides in Matisaa gray rock against those in Konza kunkur.

The fundamental oxides of cement in Konza kunkur were also found in Matisaa gray rock except SO<sub>3</sub>, Na<sub>2</sub>O, and K<sub>2</sub>O (Figure 5.2). This difference can be attributed to geo-

logical formations of the two materials. The correspondence of the oxide proportions in Matisaa gray rock and Konza kunkur shows that they can be used in place of each other. The proportion of MgO in Matisaa gray rock (1.56 - 3.56 wt.%) and Konza kunkur (1.49 – 3.35) (Table 5.2) implies that their lime nature is dolomitic ( $\text{CaMg}[\text{CO}_3]_2$ ) rather than calcitic ( $\text{Ca}[\text{CO}_3]_2$ ). Materials with this lime characteristics can be linked to a class of terrestrial limestone known as kunkur.

According to the European Standards EN 197-1, (2011); EN 206-1, (2011); and EN 450-1, (2012), the applicability and nature of cement raw materials, whether pozzolanic, hydraulic or both, is predetermined by chemical content of the fundamental oxides. EN 450-1, (2012) defines a pozzolan as a material whose content of  $\text{SiO}_2 + \text{Al}_2\text{O}_3 + \text{Fe}_2\text{O}_3 \geq 70$  wt.%. On the other hand, a hydraulic has been defined by EN 197-1, (2011) as a material whose content of  $\text{CaO} + \text{SiO}_2 \geq 50$  wt.%.

It further specifies the thresholds of the other fundamental oxides as follows:  $\text{MgO} < 4.0$  wt.%,  $\text{SO}_3 < 3.5 \leq 4.0$  wt.% and summation of  $\text{K}_2\text{O} + \text{Na}_2\text{O} \leq 4.0$  wt.%. In Matisaa gray rock, the average content of  $\text{SiO}_2 + \text{Al}_2\text{O}_3 + \text{Fe}_2\text{O}_3$  is 18.55 wt.% whereas average content of  $\text{CaO} + \text{SiO}_2$  is 58.09 wt.%, and thus Matisaa gray rock does not exhibit the potential properties of being pozzolanic but rather hydraulic regarding the thresholds specified by EN 206-1, (2011) and EN 450-1, (2012). Except for  $\text{SO}_3$ , the proportions of the alkaline oxides ( $\text{Na}_2\text{O}$ , and  $\text{K}_2\text{O}$ ) were found to be within the thresholds specified by EN 450-1, (2012).

Non-threshold proportions of the fundamental oxides of cement trigger deleterious effects. For instance, the content of  $\text{CaO} + \text{SiO}_2 < 50$  wt.% cause low levels of hydration of calcium silicates;  $\text{MgO} > 4.0$  wt.% cause delayed expansion and thus volume instability;  $\text{K}_2\text{O} + \text{Na}_2\text{O} > 4.0$  wt.% trigger the reaction of the alkalis and silicates resulting to corrosion of cement structures (Snellings et al., 2016).

## 5.2 Raw Mix Moduli of Matisaa gray rock

The measured raw mix moduli of MGR is discussed in comparison to the acceptable limits for each modulus (Hydraulic Modulus (HM), lime Saturation Factor (LSF), Silica Ratio (SR), Alumina Ratio (AR), and the Sulfatisation Modulus (SM)). These moduli were calculated from the respective cement oxides of MGR and Konza kunkur reported in Table 1.

Table 5.2: Raw mix moduli of Matisaa gray rock and Konza kunkur.

Raw material	HM	LSF	SR	AR	SM
Matisaa gray rock	2.05–2.61	0.82–0.92	2.87–13.65	0.85–4.63	1.69–3.87
Raw Konza kunkur	1.86–1.94	0.77–0.88	2.37–4.16	2.22–4.44	-

The HM of Matisaa gray rock ranges from 2.05 – 2.61. This HM value is comparable to that of raw Konza Kunkur (1.86 – 1.94) and also lies within the recommended limits ( $1.7 \leq \text{HM} \leq 2.3$  (Aldieb & Ibrahim, 2010)). The HM range Matisaa gray rock indicates that is energy efficient, free from free lime, and therefore would produce clinker of good quality. The average proportions for MGR and Konza kunkur are 2.56 and 2.42 wt.% respectively. Having values that are higher than 2.0 wt.%, Equation 3.12 was used to calculate the LSF for MGR and Konza kunkur. The respective LSF ranges obtained are 0.82 – 0.92 and 0.77 – 0.88 for MGR and Konza kunkur.

The recommended range of LSF is 0.80 – 0.98 (Hills & Johansen, 2002), which fits in that of Matisaa gray rock. This indicates that clinker from Matisaa gray rock would be easy to burn and thus energy-efficient, form complete alite and belite phases and does not contain free lime which hampers the burnability of the raw meal. LSF values higher than 0.98 imparts harder burning and thus higher fuel consumption and tends to produce unsound cement (Ahmad, 2020).

The silica ratio of Matisaa gray rock ranges from 2.87 – 13.65. This SR value is far beyond the acceptable limits ( $1.5 \leq \text{SR} \leq 3.2$  (Aldieb & Ibrahim, 2010)). It indicates that Matisaa gray rock would form high calcium silicates and less aluminate and ferrite (solid/liquid phase). This is due to the low content of  $\text{Fe}_2\text{O}_3$  and  $\text{Al}_2\text{O}_3$  in Matisaa gray

rock. This high SR value indicates that clinker from Matisaa gray rock would form by harder burning of the raw meal and thus higher energy consumption. Such high SR values also hint at the possible deterioration of the kiln lining (Ahmad, 2020), thereby necessitating the beneficiation of Matisaa gray rock for clinker production.

The AR value predicates the potential relative content of aluminate and ferrite phases in the resultant clinker (Moses & Alabi, 2016). The alumina ratio of Matisaa gray rock (0.85 – 4.63) is beyond the acceptable limits ( $1.5 \leq AR \leq 2.0$  (Aldieb & Ibrahim, 2010)). This could be due to the unproportionate content of  $Fe_2O_3$  and  $Al_2O_3$  in Matisaa gray rock. AR values higher than 2.0 tend to increase the aluminate phase at the expense of the ferrite phase, thereby compromising the clinker quality (Moses & Alabi, 2016). This also imparts harder burning which translates to high fuel consumption (Moses & Alabi, 2016). This, therefore, necessitates the beneficiation of Matisaa gray rock for clinker production.

The sulfatisation modulus of Matisaa gray rock ranges from 1.69 – 3.87. This SM value of rock is beyond the acceptable limits ( $0.8 \leq SM \leq 1.2$  (Winter, 2005)) and is attributed to the high  $SO_3$  content in Matisaa gray rock. It implies that the proportion of belite phase in clinker made from Matisaa gray rock will be lower than the proportion of alite phase, and thus low-quality clinker. Thus, beneficiation is required to harmonize the sulphur and alkalis content in Matisaa gray rock. Overall, the raw moduli values of Matisaa gray rock indicate that Matisaa gray rock can be used for clinker production provided it is beneficiated to reduce  $MgO$  and  $SO_3$ , and enrich  $Fe_2O_3$  and  $Al_2O_3$  to the required level.

### **5.3 Phase Identification Studies**

With the XRD technique, Matisaa gray rock showed two main Bragg reflection among other several reflections as depicted in Figure 5.3.



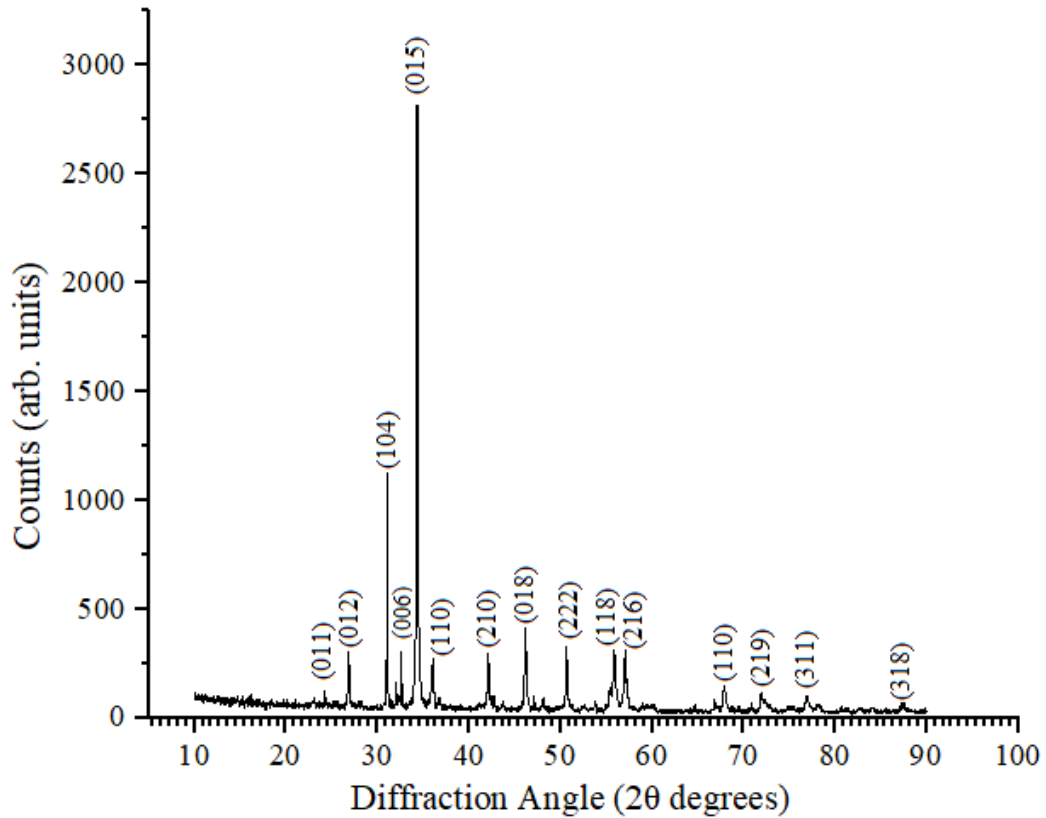


Figure 5.3: XRD spectra of Matisaa gray rock. The peak labels represent the miller indices.

Matisaa gray rock showed sharp XRD peaks with negligible background absorption. The Bragg's reflections of Matisaa gray rock were compared against calcite and dolomite. Typical XRD spectra of both calcite and dolomite show Bragg's reflections at (012), (104), (006), (110), (113), (202), (024), (018), (116), (214) and (300) (Gunasekaran et al., 2006). Dolomite is distinguished by three superstructure Bragg's reflections; (101), (015), and (021), which are systematically absent in calcite (Kaczmarek et al., 2017). Matisaa gray rock showed reflections at (011), (012), (104), (006), (015), (110), (210), (018), (222), (118), (216), (311), (219), and (318).

The most intense reflection (015) corresponds to one of the three superstructure reflections that distinguish dolomite ( $\text{CaMg}[\text{CO}_3]_2$ ) from calcite ( $\text{Ca}[\text{CO}_3]_2$ ) (Rodriguez-Blanco et al., 2015). Calcite and dolomite exhibit more or less the same crystal structures which are fundamentally different. Calcite has one crystallographically distinct cation site whereas dolomite has two independent cation sites (Kaczmarek et al., 2017). The second prominent Bragg's reflection (104) match with kutnohorite. Kutnohorite

( $\text{Ca}[\text{Mn}^{2+}, \text{Mg}, \text{Fe}^{2+}][\text{CO}_3]_2$ ) is a rare carbonate of Ca in combination with either Mn, Mg, and Fe, and it belongs to the dolomite group (Polgári et al., 2017). These phases are summarized in Figure 5.4.

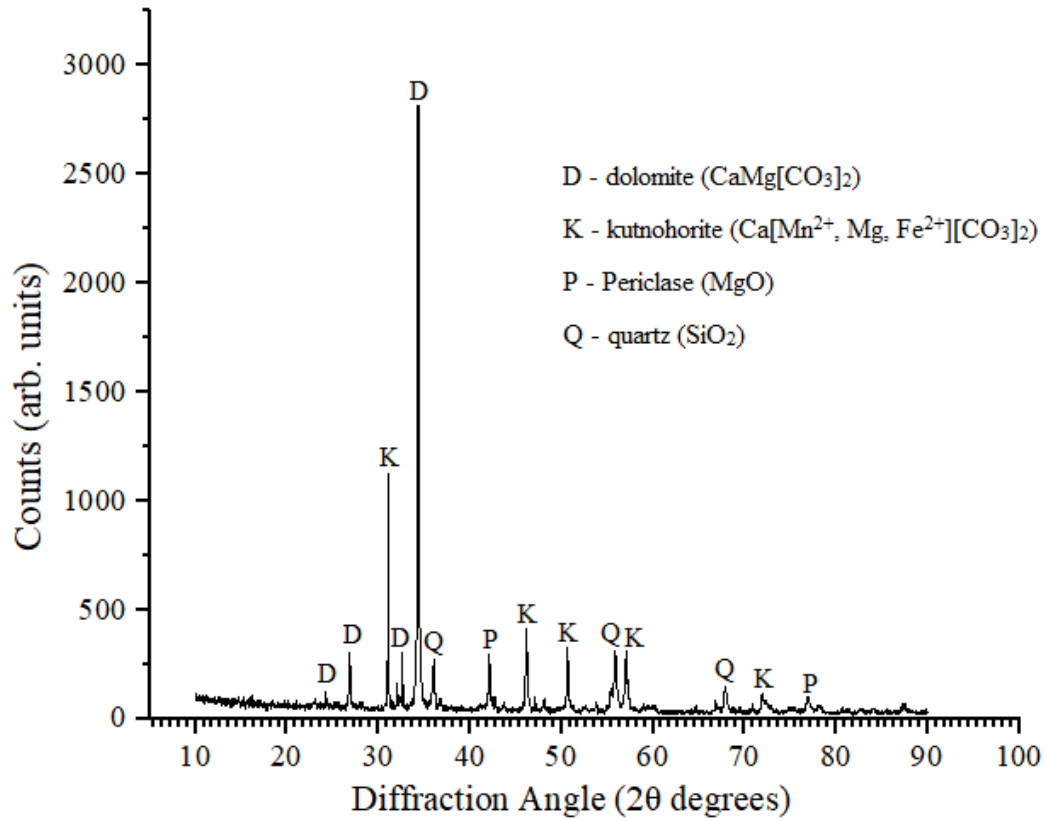


Figure 5.4: XRD crystal phases of Matisaa gray rock. The labels D, K, P, and Q represent dolomite, kutnohorite, periclase, and quartz crystal phases respectively.

The XRD pattern (Figure 5.4) shows that Matisaa gray rock is dominated by dolomite and kutnohorite with trace mineral phases of quartz and periclase. The Bragg's reflections in Matisaa gray rock compare with Konza kunkur as depicted in Figure 5.5.

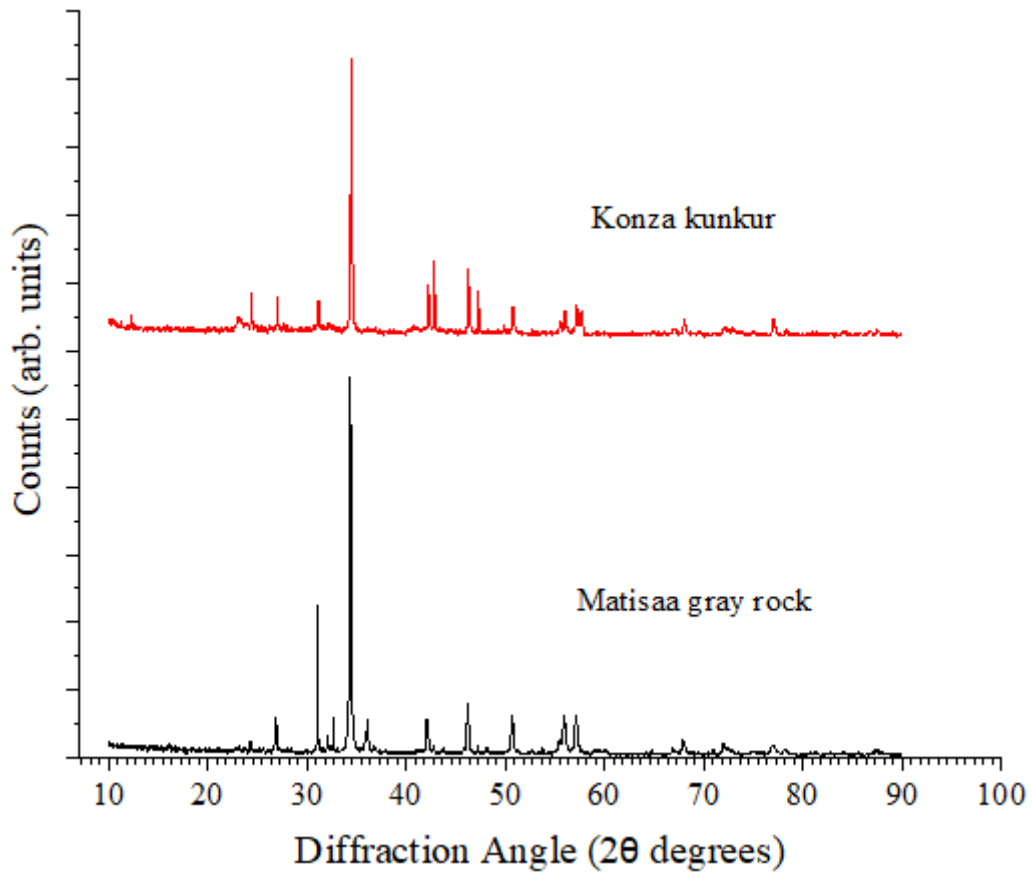


Figure 5.5: XRD diffractograms of Matisaa gray rock versus Konza kunkur.

The correspondence of the XRD patterns of Matisaa gray rock and Konza kunkur implies that both materials could be made up of more or less similar crystals. It has been established that the use of crystalline admixtures increases the durability of cement-based materials (García-Vera et al., 2018). An admixture is an ingredient that is added to the concrete just before or during mixing to improve its properties like resistance by chemical attack, setting time, workability, strength, etcetera (Ramachandran, 2001). Further, on the crystal structure, it was possible to obtain information that is complementary to XRD from Raman spectra. The Raman signatures of Matisaa gray rock are as shown in Figure 5.6.

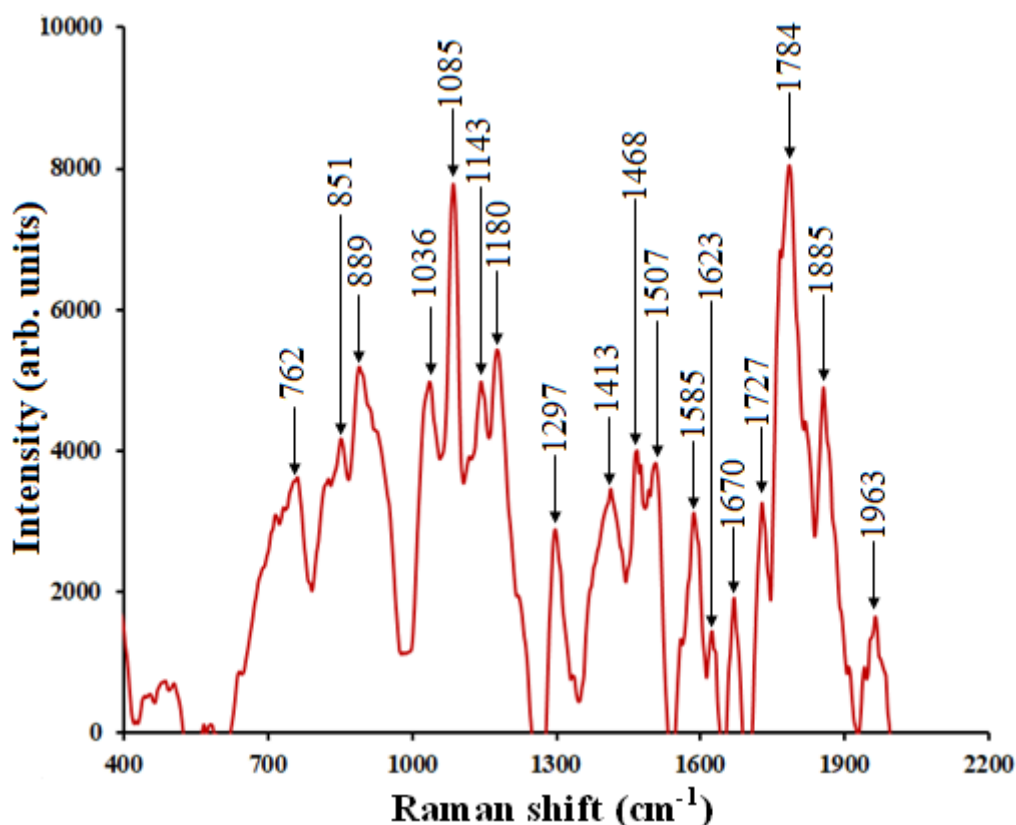


Figure 5.6: Raman spectra of Matisaa gray rock.

In Matisaa gray rock,  $\nu_1$ ,  $\nu_2$ ,  $\nu_3$ , and  $\nu_4$  were respectively observed at 1085, 1440, 889, and 762  $\text{cm}^{-1}$ . Although these vibrational modes are a characteristic of calcite, they are however much broader, degenerate, and slightly shifted compared to typical calcite. The  $\nu_1$  vibration mode (1085  $\text{cm}^{-1}$ ), is split into a triplet at 1036, 1143, and 1180  $\text{cm}^{-1}$ . The modes  $\nu_2$  (889  $\text{cm}^{-1}$ ) is split into a doublet bearing  $\nu_4$  (762  $\text{cm}^{-1}$ ) and 851  $\text{cm}^{-1}$ . Likewise,  $\nu_3$  (1140  $\text{cm}^{-1}$ ) is split into a doublet at 1413, and 1507  $\text{cm}^{-1}$ .

Degeneracy of molecular vibrational modes in  $\text{CO}_3^{2-}$  ions arises from combined effects of symmetric stretching and bending planes of the, and different site symmetries in the unit cell (Behrens et al., 2006). This explanation can further be elaborated based on the crystal structure of calcite and dolomite. Both calcite and dolomite exhibit rhombohedral crystal cleavage (Liu et al., 2014). The cationic movement of Mg and Ca in dolomite cause distortion and splitting of the carbonate groups as the crystal surfaces undergo relaxation during cationic substitution (Cygan et al., 2001).

The Raman signatures at 1032  $\text{cm}^{-1}$  are ascribed to gypsum. The main vibration modes

of gypsum structures occur at 1017 or 1025  $\text{cm}^{-1}$  (Prieto-Taboada et al., 2014). Referring to the work of Sun et al., (2014), the vibration bands at 1623 and 1670  $\text{cm}^{-1}$  are attributed to the bending mode of water molecules. Ideally, this mode occurs at 1630  $\text{cm}^{-1}$  (Sun et al., 2014). The vibration modes of 1623 and 1670 in Matisaa gray rock indicate the presence of water molecules that are bound with the  $\text{SO}_4^{2-}$  ions to form gypsum. This further indicates that the gypsum in Matisaa gray rock is in a hydrous form. For high purity calcite, the Raman vibrational modes  $\nu_1$ ,  $\nu_2$ ,  $\nu_3$   $\nu_4$  respectively occur at 1080, 870, 1450, and 700  $\text{cm}^{-1}$  (Behrens et al., 2006).

## 5.4 Morphological Studies

The morphology of Matisaa gray rock powder at micron and nano scales is shown in Figure 5.7 (a) and (b), respectively. It is seen that Matisaa gray rock comprises of irregularly shaped particles that are compact with rough superficial texture. It is also observed that the cleavage planes of the particles are smooth with blocky edges as pointed by arrows in Figure 5.7.

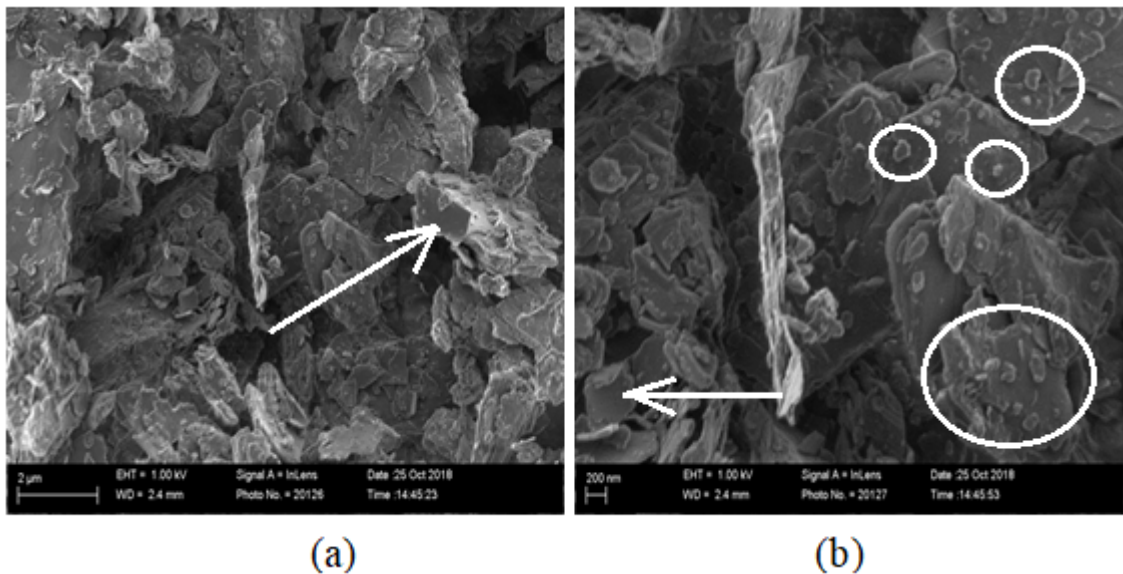


Figure 5.7: SEM micrographs of Matisaa gray rock: (a) and (b) scanned at resolutions of 2  $\mu\text{m}$  and 200 nm respectively.

These characteristics, working together indicates that the resultant cement from Matisaa (without beneficiation) would require more water to hydrate and take longer to form

a workable mass. However, the rough surface texture is an indicator of good adhesion with cement aggregates. Limestone-based minerals are characterized by particles with rhombohedron-shaped compact surfaces (De Souza & Bragança, 2017). These particles, however, generally vary in shape with the majority being irregular and some being rounded (spherical) due to ball milling. In hydration kinetics, irregular-shaped particles result in poor packing density which demands more water to hydrate, whereas low porosity calls for longer times to attain the required workability (Ooi et al., 2015). At a closer inspection of Figure 5.7, it is noted that there are much smaller particles which are sparsely distributed in the microstructure of Matisaa gray rock. These particles are clearer at the nano-scale, as encircled in Figure 5.7 (b). The sparse distribution of these smaller particles points out that Matisaa gray rock has little tendency to form secondary particles (the agglomerates). It is established that nano-size particles of calcium carbonate materials easily agglomerate due to their high surface energy (Yang & Che, 2018). Agglomeration compromises the properties of cementitious materials, posing a challenge in their applications (Meng et al., 2017).

## **5.5 Particle Size Distribution**

The particle size of Matisaa gray rock and Konza kunkur compares as shown in Figure 5.9.

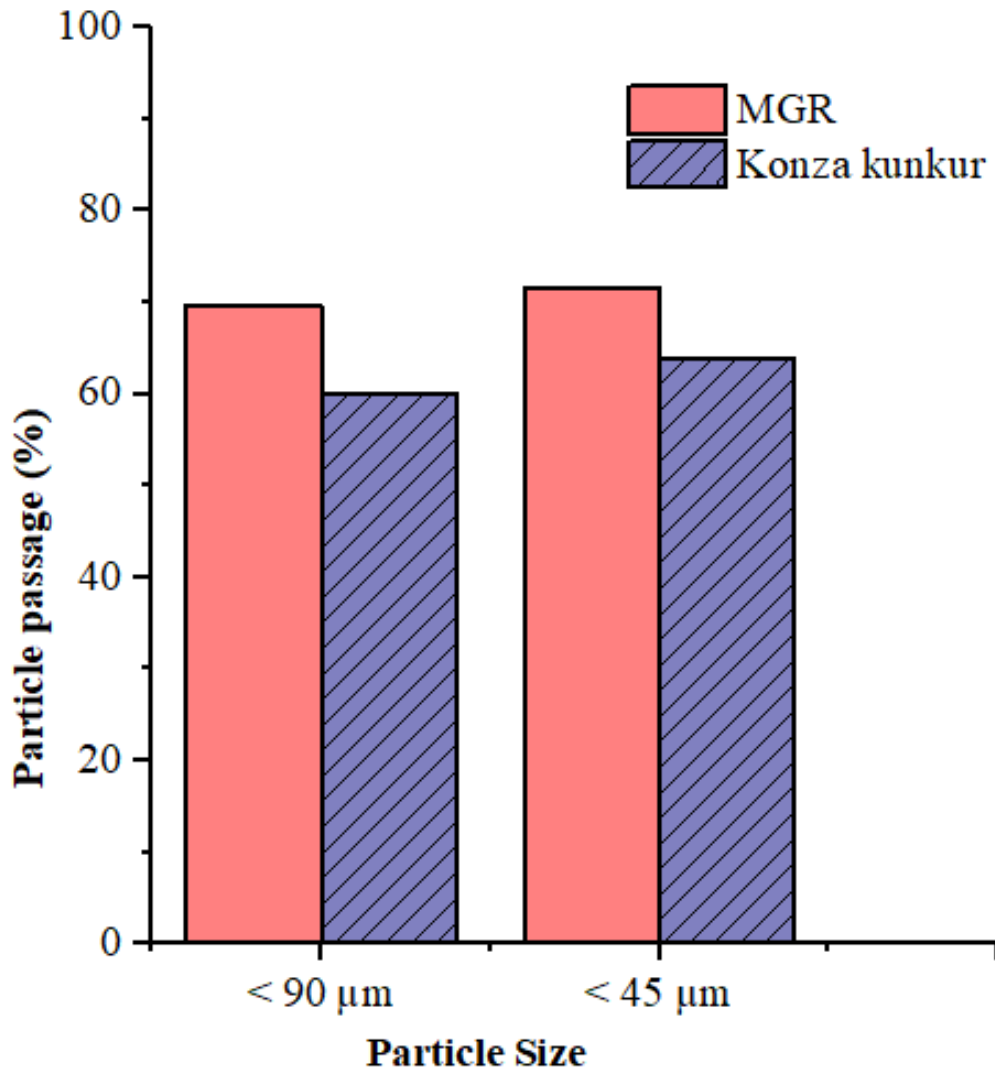


Figure 5.8: A comparative bar graph of particle passage analysis of Matisaa gray rock against Konza kunkur. MGR stands for Matisaa gray rock.

69.65% of the particle size composition of Matisaa gray rock was found to be  $<90 \mu\text{m}$ . Out of this composition, 71.60% of the particle sizes were  $<45 \mu\text{m}$ . This particle size distribution was comparable to that of Konza kunkur as depicted in figure 5.8. According to the ASTM C618 - 05 standard, for proper hydration kinetics of natural pozzolans to occur,  $\geq 66\%$  of the particles should be  $<45 \mu\text{m}$ -sized.

### 5.5.1 Specific Surface Area (SSA)

The SSA of Matisaa gray rock and that of Konza kunkur is as shown in Figure 5.9.

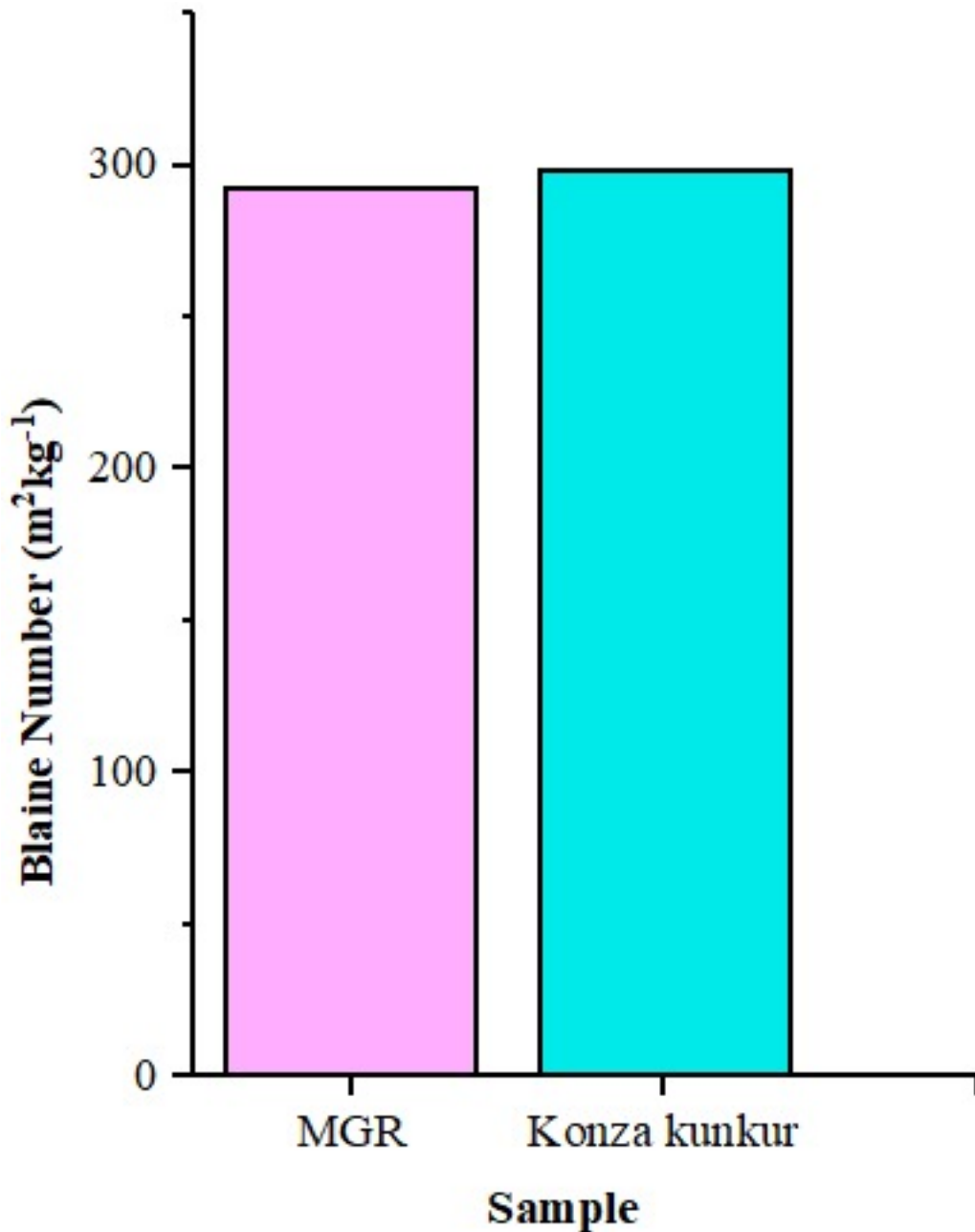


Figure 5.9: A comparative bar graph of the SSA of Matisaa gray rock against Konza kunkur cement. MGR stands for Matisaa gray rock.

The SSA of the two materials are 292.5 m<sup>2</sup>/kg and 298.3 m<sup>2</sup>/kg, indicating that both Matisaa gray rock and Konza kunkur require comparable amount of energy to attain the same specific surface area. The specific surface area for many cement raw materials has been found to range between 250 – 450 m<sup>2</sup>/kg (Goncharenko et al., 2018). Therefore, in this regard, the specific surface area of Matisaa gray rock corroborates that of established cement raw materials.



## CHAPTER 6

### SUMMARY, CONCLUSIONS, AND RECOMMENDATIONS

#### 6.0 Introduction

This chapter summarizes the key findings of this study and elucidates cement potential of Matisaa gray rock. The chapter ends by giving recommendations to further this research.

#### 6.1 Summary

Some of the cement raw materials that are still used to date were discovered many centuries ago. However, due to high population growth rates and the pressure in building durable structures, the deposits of these raw materials have been reported to deplete at faster rates. Some companies that consume large amounts of these materials like East African Portland Cement Company Ltd. (EAPCC), Athi River, Kenya have already sought an alternative material for crystalline limestone. The present study has characterized Matisaa gray rock for the same purpose.

In the present work, the mineralogical properties of Matisaa gray rock have been found and correlated with its established counterparts, based on a database collected from the literature and with data from actual materials. Matisaa gray rock was found to contain the following major oxides of cement: CaO, SiO<sub>2</sub>, Al<sub>2</sub>O<sub>3</sub>, Fe<sub>2</sub>O<sub>3</sub>, and MgO arranged in the order of most dominant to the least. Among the minor oxides that were present in Matisaa gray rock include K<sub>2</sub>O, Na<sub>2</sub>O, and SO<sub>3</sub>. The mineralogical composition and morphology of Matisaa gray rock were found to match the properties of other materials that are already used in cement manufacture. The main mineral phases found in Matisaa gray rock are dolomite, kutnohorite, quartz, and periclase.

The lime-rich dolomitic composition and terrestrial location of Matisaa gray rock can be related to kunkur. Kunkur refers to non-sedimentary materials that are predominantly but not exclusively calcareous, occurring in arid and semiarid environments. It

occurs as weathered crust consisting of a mixture of silica, calcite, dolomite, ferric oxide, and gypsum, and thus generally referred to as “surface limestone” or “calcareous duricrust.”

## 6.2 Conclusions

Based on the present work the following conclusions can be drawn:

(1) Matisaa gray rock was found to contain all the oxides of cement in the following percentage abundances: 39.03 – 42.73 wt.% for CaO, 15.68 – 16.79 wt.% for SiO<sub>2</sub>, 0.47 – 4.81 wt.% for Al<sub>2</sub>O<sub>3</sub>, 0.55 – 1.04 wt.% for Fe<sub>2</sub>O<sub>3</sub>, 1.56 – 3.56 wt.% for MgO, 3.30 – 6.06 wt.% for SO<sub>3</sub>, 0.11 – 0.21 wt.% for Na<sub>2</sub>O, and 0.59 – 2.64 wt.% for K<sub>2</sub>O. Except for SO<sub>3</sub>, the proportions of the remaining oxides were found to be within the recommended thresholds.

The mineral phases found in Matisaa gray rock are dolomite (CaMg[CO<sub>3</sub>]<sub>2</sub>) and kutnohorite (Ca[Mn<sup>2+</sup>, Mg, Fe<sup>2+</sup>][CO<sub>3</sub>]<sub>2</sub>) mineral phases with trace phases of quartz (SiO<sub>2</sub>) and periclase (MgO). It has all the primary minerals (CaO, SiO<sub>2</sub>, Al<sub>2</sub>O<sub>3</sub>, Fe<sub>2</sub>O<sub>3</sub>) of cement within the recommended thresholds.

(2) The morphology of Matisaa gray rock powder comprises of irregularly shaped particles that are compact with rough superficial texture, characteristic of limestone-based materials.

(3) 69.65% of the particle size composition of Matisaa gray rock was found to be <90 μm. Out of this composition, 71.60% of the particle sizes were <45 μm, contributing to a specific surface area of 292.5 m<sup>2</sup>/kg which is within the SSA range for cement raw materials.

Its general comparison with cement properties of Konza kunkur suggests that Matisaa gray rock has potential for utilization in the manufacture of cement.

### **6.3 Recommendations for Further Study**

There could be more work that is primary to qualifying Matisaa gray rock as a cement raw material, and therefore the following recommendations have been put forward for further research:

- (1) Determination of harmful compounds in Matisaa gray rock. While the chemical study of Matisaa gray rock focused only on elements and compounds that are essential in the manufacture of cement, it could be possible that the rock contains compounds that are deleterious to the environment when subjected to calcination temperatures of cement.
- (2) After protocols that require manufacture have been finalized, prototype cement will be manufactured from Matisaa gray rock and characterized for compliance with ASTM standard for Ordinary Portland cements.

## REFERENCES

- Abdunnabi, A. R. (2012). XRF Analysis of Portland Cement for Major and Trace Elements. *Eleveth Arab Conference on the Peaceful Uses of Atomic Energy, Khartoum, Sudan*, 1–15.
- Ahmad, F. (2020). Industrial scale kiln problems and their solution with controlling different operating parameters. *Austin Chemical Engineering*, **7(1)**, 1–9.
- Ahmed, T., and Mohammed, M. (2012). Composition and phase mineral variation of Portland cement in Mass Factory Sulaimani – Kurdistan Region NE- Iraq. *International Journal of Basic and Applied Sciences*, **12(6)**, 109–118.
- Akpan, I. O., Amodu, A. E., and Akpan, A. E. (2011). Elemental analysis of limestone samples from Obajana and Mfamosing limestone deposits, Nigeria, using nuclear techniques. *Applied Radiation and Isotopes*, **69(10)**, 1355–1358.
- Aldieb, M. A., and Ibrahim, H. G. (2010). Variation of Feed Chemical Composition and Its Effect on Clinker Formation-Simulation Process. *Proceedings of the World Congress on Engineering and Computer Science*, **2**, 1–7.
- Alegbe, J., Ayanda, O. S., Ndungu, P., Alexander, N., Fatoba, O. O., and Petrik, L. F. (2018). Chemical, Mineralogical and Morphological Investigation of Coal Fly Ash Obtained from Mpumalanga Province, South Africa. *Research Journal of Environmental Sciences*, **12(3)**, 98–105.
- Alkhateeb, R. (2013). Chemical analysis of ordinary portland cement of Iraq. *International Journal of Chemical & Petrochemical Technology (IJCPT)*, **4(1)**, 23–30.
- Al-Mansour, A., Chow, C. L., Feo, L., Penna, R., and Lau, D. (2019). Green concrete: By-products utilization and advanced approaches. *Sustainability (Switzerland)*, **11(19)**, 1–30.
- Angelescu, N., Stancu, C., Amziane, S., Bratu, V., and Valentina, S. E. (2017). Study on Hydration and Strengthening of High Alumina Cements. *Scientific Bulletin of Valahia University - Materials and Mechanics*, **15(12)**, 22–27.
- Arvaniti, E. C., Juenger, M. C. G., Bernal, S. A., Duchesne, J., Courard, L., Leroy, S., and De Belie, N. (2014). Determination of particle size, surface area, and shape of supplementary cementitious materials by different techniques. *Materials and Structures/Materiaux et Constructions*, **48(11)**, 3687–3701.
- Arvaniti, E. C., Juenger, M. C. G., Bernal, S. A., Duchesne, J., Courard, L., Leroy, S., and De Belie, N. (2015). Physical characterization methods for supplementary cementitious materials. *Materials and Structures/Materiaux et Constructions*, **48(11)**, 3675–3686.

- ASTM C204-07. (2007). Designation: C204-07 Standard Test Methods for Fineness of Hydraulic Cement by Air-Permeability Apparatus. *American Society for Testing and Material*, 1–9.
- ASTM C618-05. (2005). Standard Specification for Coal Fly Ash and Raw or Calcined Natural Pozzolan for Use in Concrete. *ASTM International, West Conshohocken, PA, www.astm.org*.
- ASTM C618-12a. (2012). Standard specification for coal fly ash and raw or calcined natural pozzolan for use in concrete. *ASTM International, West Conshohocken, PA, www.astm.org*
- Atiemo, E.(2012). Studies on the Effect of Selected Local Admixtures on Essential Properties of Cement for Housing Construction. *PhD Thesis*, Kwame Nkrumah University of Science and Technology, 1–149.
- Behrens, G., and Ubic, R. (2006). Spectroscopy Letters: An International Journal for Rapid Raman Spectra of Vateritic Calcium Carbonate. *Spectroscopy Letters*, **28(6)**, 983–995.
- Bouyahyaoui, A., Cherradi, T., Abidi, M. L., and Tchamdjou, W. H. J. (2018). Characterization of Particle Shape and Surface Properties of Powders from Volcanic Scoria. *Journal of Materials and Environmental Science*, **9 (7)**, 2032–2041.
- Cardoso, R., Ribeiro, D., and Néri, R. (2017). Bonding effect on the evolution with curing time of compressive and tensile strength of sand-cement mixtures. *Soils and Foundations*, **57(4)**, 655–668.
- Celik, I. B. (2009). The effects of particle size distribution and surface area upon cement strength development. *Powder Technology*, **188(3)**, 272–276.
- Chavarria, Daniella, J., Ticzon, L. V. L., Maridel, B. A., and Patrick, C. K. (2014). Housing and Basic Needs, 1–14.
- Chhorn, C., Hong, S. J., and Lee, S. W. (2018). Relationship between compressive and tensile strengths of roller-compacted concrete. *Journal of Traffic and Transportation Engineering (English Edition)*, **5(3)**, 215–223.
- CiMSA. (2017). Effects of Particle Size Distribution on Performance in Cementitious Systems. *Cement Research and Application Center*, 1–17.
- Consoli, N. C., Festugato, L., Gravina, C., and Cruz, R. C. (2013). Key parameters for strength control of rammed sand – cement mixtures: Influence of types of portland cement. *Construction and Building Materials*, **49**, 591–597.
- Cygan, R. T., Wright, K., Fisler, D. K., Gale, J. D., and Slater, B. (2001). Atomistic models of carbonate minerals: Bulk and surface structures, defects, and diffusion. *Journal of Molecular Simulation*, **28(6)**, 475–495.

- De Souza, F., and Bragança, S. R. (2017). Evaluation of limestone impurities in the desulfurization process of coal combustion gas. *Brazilian Journal of Chemical Engineering*, **34**(1), 263–272.
- Dey, S., Sahu, L., Chaurasia, B., and Nayak, B. (2020). Prospects of utilization of waste dumped low-grade limestone for iron making: A case study. *International Journal of Mining Science and Technology*, 1–13.
- Dhir, R. K., Brito, J. de, Mangabhai, R., and Lye, C.Q. (2017). Copper Slag in Cement Manufacture and as Cementitious Material. *Sustainable Construction Materials*, 165–209.
- Dishman, K. L. (2006). Sieving in Particle Size Analysis. *Encyclopedia of Analytical Chemistry: Applications, Theory and Instrumentation*. John Wiley & Sons, Ltd, 1–35.
- Ding, Y., Dai, J., and Shi, C. (2018). Fracture properties of alkali-activated slag and ordinary Portland cement concrete and mortar. *Construction and Building Materials*, **165**, 310–320.
- Dukic, D., Lazic, D., Drljaca, D., and Imamovic, M. (2018). Characterization of raw materials and final product in the cement production. *Bulletin of the Chemists and Technologists of Bosnia and Herzegovina*, **51**, 47–52.
- EN 197-1. (2011). Cement – Part 1: Composition, specifications and conformity criteria for common cements.
- EN 206 -1. (2011). Concrete – Materials – Rules for application of EN 206-1 in Denmark.
- EN 450 -1. (2012). Fly ash for concrete – Part 1: Definition, specifications and conformity criteria.
- Fan, Q. (2012). A new method of calculating interplanar spacing: The position-factor method. *Journal of Applied Crystallography*, **45**(6), 1303–1308.
- Gaber, M. A. W. (2018). Characterizations of El Minia limestone for manufacturing paper filler and coating. *Egyptian Journal of Petroleum*, **27**(4), 437–443.
- Gao, T., Shen, L., Shen, M., Liu, L., and Chen, F. (2015). Analysis of material flow and consumption in cement production process. *Journal of Cleaner Production*, **112**, 553–565.
- García-Vera, V. E., Tenza-Abril, A. J., Saval, J. M., and Lanzón, M. (2018). Influence of crystalline admixtures on the short-term behaviour of mortars exposed to sulphuric acid. *Materials*, **12**(1), 1–16.

- Gmbh, S. (2018). Monitoring Fineness of Raw Meal and Cement by Grain Size Distribution. *Lea's Chemistry of Cement and Concrete, Elsevier Ltd*, 1–8.
- Goncharenko, D., Bondarenko, D., and Starkova, O. (2018). Repair and refurbishment technologies for inspection shafts in deep-level sewer tunnels. *World Journal of Engineering*, **15(1)**, 48–53.
- Government of the Republic of Kenya. (2007). The Kenya Vision 2030. The Popular Version, 1–32.
- Gunasekaran, S., Anbalagan, G., and Pandi, S. (2006). Raman and infrared spectra of carbonates of calcite structure. *Journal of Raman Spectroscopy*, **37(9)**, 892–899.
- Hills, L., and Johansen, V. (2002). Burning the mix. *International Cement Journal*, 79–84.
- Hsu, S., Chi, M., and Huang, R. (2018). Effect of fineness and replacement ratio of ground fly ash on properties of blended cement mortar. *Construction and Building Materials*, **176**, 250–258.
- <https://www.capitalfm.co.ke/business/2020/01/government-urged-to-impose-25pc-duty-on-imported-cement-raw-materials/> Accessed on 11<sup>th</sup> November 2020 at 8.30 PM, South African Time.
- Jo, B., Chakraborty, S., and Yoon, K. W. (2014). A hypothetical model based on the effectiveness of combined alkali and polymer latex modified jute fibre in controlling the setting and hydration behaviour of cement. *Construction and Building Materials*, **68**, 1–9.
- Johari, A. (2015). Kenya's Konza Techno City: Utopian Vision Meets Social Reality Social Reality. *SIT Digital Collections*, 1–68.
- Juenger, M., Provis, J. L., Elsen, J., Matthes, W., Hooton, R. D., Duchesne, J., Courard, L., He, H., Michel, F., Snellings, R., and Belie, N. D. (2012). Supplementary Cementitious Materials for Concrete: Characterization Needs. *Materials Research Society*, **1488**, 2–16.
- Kaczmarek, S. E., Gregg, J. M., Bish, D. L., Machel, H. G., and Fouke, B. W. (2017). Dolomite, very high-magnesium calcite, and microbes implications for the microbial model of dolomitization. *SEPM Special Publications*, **109**, 1–14.
- Karstensen, K. H. (2006). Cement Production in Vertical Shaft Kilns in China: Status and Opportunities for Improvement. *Report to the United Nations Industrial Development Organization*, 1–32.
- Kenya Vision 2030. (2007). Africa Research Bulletin: Economic, Financial and Technical Series. 1–29.

- Khandaker, M., Parvej, M. S., and Kallol, K. M. Z. (2018). Effect of Curing Time on the Mechanical Properties of a Veterinarian Bone Cement. *AIP Conference Proceedings*, 2–8.
- Kenya National Bureau of Statistics (KNBS) Report. (2018). Kenyan cement consumption falls for first time since 2000, *Global Cement News*.
- Kinyua, L. (2013). Pozzolana Cement Obtained by Calcining Raw Clays/Rice Husks Mixtures. *MSc. Thesis*, Kenyatta University, 6–51.
- Koehler, E. P., and Fowler, D. W. (2003). Summary of concrete workability test methods. *International Center for Aggregates Research*, 1–73.
- Krivoborodov, Y., and Samchenko, S. (2019). Synthesis of high alumina cement based on metallurgy wastes. *IOP Conference Series: Materials Science and Engineering*, **687**, 1–7.
- Kruczek, B. (2014). Carman–Kozeny Equation. *Encyclopedia of Membranes*. Springer, 1–3.
- Leng, Y. (2013). Materials characterization: introduction to microscopic and spectroscopic methods. *John Wiley & Sons*, 2<sup>nd</sup> Edition, 1–392.
- Le Pevelen, D. D. (2016). X-ray crystallography of small molecules: Theory and workflow. *Encyclopedia of Spectroscopy and Spectrometry*, 624–639.
- Liu, H., Sun, Q., Wang, B., Wang, P., and Zou, J. (2016). Morphology and composition of microspheres in fly ash from the Luohuang Power Plant, Chongqing, South Western China. *Journal of Minerals*, **6(2)**, 1–10
- Liu, S., Li, H., and Liu, J. (2014). Reliability of the structural data for calcite and dolomite extracted from X-ray powder diffraction by Rietveld refinement. *An International Journal of Mineralogy, Crystallography, Geochemistry, Ore Deposits, Petrology, Volcanology and applied topics on Environment, Archeometry and Cultural Heritage*, **83(1)**, 121–140.
- Lohumi, S., Kim, M. S., Qin, J., and Cho, B. K. (2017). Raman imaging from microscopy to macroscopy: Quality and safety control of biological materials. *TrAC - Trends in Analytical Chemistry*, **93**, 183–198.
- Lothenbach, B., Scrivener, K., and Hooton, R. D. (2011). Supplementary cementitious materials. *Cement and Concrete Research*, **41**, 1244–1256.
- Luo, L., Zhang, Y., Bao, S., and Chen, T. (2016). Utilization of Iron Ore Tailings as Raw Material for Portland Cement Clinker Production. *Advances in Materials Science and Engineering*, **2016**, 1–6.
- Mavroulidou, M., Morrison, T., Unsworth, C., and Gunn, M. J. (2015). Properties of concrete made of multicomponent mixes of low-energy demanding binders. *Construction and Building Materials*, **101**, 1122–1141.



- Mbongwe, T., Nyagol, B. O., Amunkete, T., Humavindu, M., Khumalo, J., Nguruse, G., and Chokwe, E. (2014). Understanding competition at the regional level: an assessment of competitive dynamics in the cement industry across Botswana, Kenya, Namibia, South Africa, Tanzania, and Zambia. *Draft paper for presentation at pre-ICN conference*, 2–33.
- Meng, T., Yu, Y., and Wang, Z. (2017). Effect of nano-  $\text{CaCO}_3$  slurry on the mechanical properties and micro-structure of concrete with and without fly ash. *Composites Part B: Engineering*, **117**, 124–129.
- Meyer, C. (2015). Carbon Nanotubes, 1–23.
- Mikla, V. I., and Mikla, V. V. (2014). Raman Spectroscopy in Medicine. *Medical Imaging Technology, Elsevier*, 129 – 141.
- Mohammed, S., and Safiullah, O. (2018). Optimization of the  $\text{SO}_3$  content of an Algerian Portland cement: Study on the effect of various amounts of gypsum on cement properties. *Construction and Building Materials*, **164**, 362–370.
- Morelhão, S. K. (2016). Fundamentals of X-Ray Physics. In book: Computer Simulation Tools for X-ray Analysis. 1–57.
- Moses, N. E, and Alabi, S. B. (2016). Predictive model for cement clinker quality parameters. *Journal of Materials Science and Chemical Engineering*, **04(07)**, 84–100.
- Mounia, B., Merzoug, B., Chaouki, B., and Djaouza, A. A. (2013). Physico-Chemical Characterization of Limestones and Sandstones in a Complex Geological Context. *IACSIT International Journal of Engineering and Technology*, **5(1)**, 114–118.
- Naqi, A., and Jang, J. G. (2019). Recent progress in green cement technology utilizing low-carbon emission fuels and raw materials: *Journal of Sustainability, Switzerland*, **11(2)**, 1–18.
- Niesel, K. (1973). Determination of the specific surface by measurement of permeability. *Mat. Constr.*, **6**, 227–231.
- Obiajunwa, E. I., and Nwachukwu, J. I. (2000). Elemental analysis of limestone samples from Ewekoro limestone deposit in southwest Nigeria. *Nuclear Instruments and Methods in Physics Research*, **170(3)**, 427–431.
- Ooi, Z. X., Ismail, H., and Bakar, A. A. (2015). Characterization of oil palm ash (OPA) and thermal properties of OPA-filled natural rubber compounds. *Journal of Elastomers and Plastics*, **47(1)**, 13–27.
- Oye, B. (2012). Wood ash as raw material for Portland cement. *SINTEF Materials and Chemistry*, 1–16.

- Paine, K. A. (2019). Physicochemical and mechanical properties of Portland cements. *Lea's Chemistry of Cement and Concrete. Elsevier Ltd., 5<sup>th</sup> Ed.*, 285- 339.
- Park, R. (2003). Concrete, Reinforced, *Encyclopedia of Physical Science and Technology*, 3<sup>rd</sup> Edition, 583-602.
- Polgári, M., Bajnóczi, B., Kovács, K. V., Götze, J., Dobosi, G., Tóth, M., and Vigh, T. (2007). Mineralogical and cathodoluminescence characteristics of Ca-rich kutnohorite from the Úrkút Mn-carbonate mineralization, Hungary. *Mineralogical Magazine*, **71(5)**, 493–508.
- Pope, C. G. (1997). X-ray diffraction and the Bragg equation. *Journal of Chemical Education*, **74(1)**, 129–131.
- Prieto-taboada, N., Larrañaga, A., Gómez-laserna, O., and Martínez-arkarazo, I. (2015). Raman spectroscopy for the characterization of the  $\text{CaSO}_4 - \text{H}_2\text{O}$  system compounds. *American Chemical Society*, **122**, 102–109.
- Ramachandran, S .V. (2001). Handbook of Analytical Techniques in Concrete Science and Technology: Principles, Techniques, and Applications. *William Andrew Publishing*, 1 – 62.
- Rao, D. S., Vijayakumar T.V., Rao, S. S., Prabhakar, S., and Raju, G. B. (2014). Cell and column flotation studies of a low grade siliceous mine waste limestone sample for cement making. *Journal of Solid Waste Technology and Management*, **40(3)**, 233–242.
- Rao, D. S., Vijayakumar, T.V., Prabhakar, S., and Raju, G. B. (2011). Geochemical assessment of a siliceous limestone sample for cement making. *Chinese Journal of Geochemistry*, **30(1)**, 33–39.
- Rao, D. S., Vijayakumar, T.V., Rao, S. S., Prabhakar, S., and Raju, G. B. (2009). Beneficiation of a siliceous limestone sample. *At Mineral Processing*, **50(6)**, 36–47.
- Reiterman, P., Holčapek, O., Jogl, M., and Konvalinka, P. (2015). Physical and Mechanical Properties of Composites Made with Aluminous Cement and Basalt Fibers Developed for High Temperature Application. *Advances in Materials Science and Engineering*, 1–10.
- Richardson, I. G. (2008). The calcium silicate hydrates. *Cement and Concrete Research*, **38(2)**, 137–158.
- Rodríguez, O., Kacimi, L., López-delgado, A., Frías, M., and Guerrero, A. (2013). Characterization of Algerian reservoir sludges for use as active additions in cement: New pozzolans for eco-cement manufacture. *Construction and Building Materials*, **40**, 275–279.

- Rodriguez-Blanco, J. D., Shaw, S., and Benning, L. G. (2015). A route for the direct crystallization of dolomite. *American Mineralogist*, **100**(5), 1172–1181.
- Schmidt, M. K., Esteban, R., González-Tudela, A., Giedke, G., and Aizpurua, J. (2016). Quantum Mechanical Description of Raman Scattering from Molecules in Plasmonic Cavities. *ACS Nano*, **10**(6), 6291–6298.
- Schneider, M., Romer, M., Tschudin, M., and Bolio, H. (2011). Cement and Concrete Research Sustainable cement production — present and future. *Journal of Cement and Concrete*, **41**(7), 642–650.
- Schramm, R. (2000). Chemometric Methods in Energy Dispersive X-Ray Fluorescence. *Analytica Chimica Acta*, **420**(2), 197–203.
- Shackley, M. S. (2011). An Introduction to X-Ray Fluorescence (XRF) Analysis in Archaeology. *Springer, New York, NY*, 7–44.
- Siebert, F., and Hildebrandt, P. (2008). Theory of Infrared Absorption and Raman Spectroscopy. *Vibrational Spectroscopy in Life Science*, 11–60.
- Šiler, P., Kolářová, I., Bednárek, J., Janča, M., Musil, P., and Opravil, T. (2018). The possibilities of analysis of limestone chemical composition. *IOP Conference Series: Materials Science and Engineering*, **379**(1), 1–6.
- Simonsen, A. M. T., Solismaa, S., Hansen, H. K., and Jensen, P. E. (2020). Evaluation of mine tailings' potential as supplementary cementitious materials based on chemical, mineralogical and physical characteristics. *Journal of Waste Management*, **102**, 710–721.
- Singh, H., and Cai, J. (2019). Permeability of Fractured Shale and Two-Phase Relative Permeability in Fractures. *Elsevier*, 105–132.
- Sjögren, C. (2018). IR spectroscopy for vibrational modes. A semi-classical approach based on classical electrodynamics and modern quantum mechanics. 1–50.
- Snellings, R. (2016). Assessing, Understanding and Unlocking Supplementary Cementitious Materials. *RILEM Technical Letters*, **1**, 1–50.
- Sousa R, and Marie S. (1998). Expansive cement blend for use in shrinkage compensating mortars. *Materials and Structures*, **31**, 400–404.
- Splinter, E., and Van Leynseele, Y. (2019). The conditional city: emerging properties of Kenya's satellite cities. *International Planning Studies*, **24**(3), 308–324.
- Sun, J., Wu, Z., Cheng, H., Zhang, Z., and Frost, R. L. (2014). A Raman spectroscopic comparison of calcite and dolomite. *Molecular and Biomolecular Spectroscopy*, **117**, 158–162.

- Trejo, D., and Prasittisopin, L. (2015). Chemical transformation of rice husk ash morphology. *ACI Materials Journal*, **112(3)**, 385–392.
- Tutur, N., and Noor, R. N. H. R. M. (2018). The Potential of Rice Husk Ash (RHA) and Coconut Fiber (CF) as Partial Replacement of Cement. *Advances in Civil Engineering and Science Technology*, 1–6.
- Uo, M., Wada, T., and Sugiyama, T. (2015). Applications of X-ray fluorescence analysis (XRF) to dental and medical specimens. *Japanese Dental Science Review*, **51(1)**, 2–9.
- Uson, A.A., López-Sabirón, A. M., Ferreira, G., and Sastresa, E. L. (2013). Uses of alternative fuels and raw materials in the cement industry as sustainable waste management options. *Renewable and Sustainable Energy Reviews*, **23**, 242–260.
- Valério, A., and Morelhão, S. L. (2019). Usage of Scherrer's formula in X-ray diffraction analysis of size distribution in systems of monocrystalline nanoparticles. 1–9.
- Wabwile, J. M. (2018). Laser Raman Microspectrometric Assessment of Uranium Forensics. *MSc. Thesis*, University of Nairobi, 1–135.
- Wanderi, M. P., and Makandi, L. (2019). Kenyan Universities Contribution Towards the President's 'Big Four' Agenda: The Case of Mount Kenya University's Graduate Enterprise Academy, 202–216.
- Wang, S., Wu, J., Wu, X., Yang, W., and Yu, B. (2016). The Use of Supersulfated Cement (SSC) in Mass Concrete. *MATEC Web of Conferences*, pp. 1–7.
- West, M., Ellis, A. T., Kregsamer, P., Potts, P. J., Strelt, C., Vanhoof, C. and Wobrauschek, P. (2010). Atomic spectrometry update – X-ray fluorescence spectrometry. *Journal of Analytical and Atomic Spectrometry*, **22(10)**, 1304–1332.
- Winter, N. B. (2005). Clinker: Compositional Parameters. *Understanding Cement*, 46–195.
- Worrell, E., Price, L., Martin, N., Hendriks, C., and Meida, L. O. (2001). Carbon Dioxide Emissions from the Global Cement Industry. *Annual Review of Energy and the Environment*, **26**, 303–329.
- Yang, H., and Che, Y. (2018). Effects of Nano- CaCO<sub>3</sub> /Limestone Composite Particles on the Hydration Products and Pore Structure of Cementitious Materials. *Advances in Materials Science and Engineering*, **2018(3)**, 1–8.
- Yildirim, I. Z., and Prezzi, M. (2011). Chemical, Mineralogical, and Morphological Properties of Steel Slag. *Advances in Civil Engineering*, **2011**, 1–13.

- Yin, H., Hou, Z., Zhang, L., Zhang, X., Wang, Z., and Li, Z. (2016). Cement raw material quality analysis using laser-induced breakdown spectroscopy, *Journal of Analytical Atomic Spectrometry*, **31(12)**, 2384–2390.
- Zhang, H. (2011). In Woodhead Publishing Series in Civil and Structural Engineering, *Building Materials in Civil Engineering*, 46–423.
- Zhou, J., and Wang, H. (2003). The physical meanings of 5 basic parameters for an X-ray diffraction peak and their application. *Chinese Journal of Geochemistry*, **22(1)**, 38–44.
- Zhu, D., Mobasher, B., and Rajan, S. D. (2012). Cement and Concrete Composites Non-contacting strain measurement for cement-based composites in dynamic tensile testing. *Cement and Concrete Composites*, **34(2)**, 147–155.

## APPENDICES

### Appendix I: Conference Presentations

This work has been presented in the following international conferences:

1. The 2<sup>nd</sup> Biennial Conference on the State of Higher Education. *Positioning Universities as the Nexus of Research, Innovation and Technology Transfer for Socio-economic Transformation*, Kenya School of Monetary Studies, Kenya, **30<sup>th</sup> October–2<sup>nd</sup> November 2018**.
2. ANSO-MMU-SAJOREC International Conference. *Biodiversity in Drylands and Wetlands: Challenges and Opportunities in the 21<sup>st</sup> Century*, Maasai Mara University, Kenya, **4–6 September 2019**.

### Appendix II: List of Publications

1. Geoffrey, M., Isaac, M., and Fredrick, O. (2020). Parametric Study of Matisaa Gray Rock as a Potential Clinker Material. *Asian Journal of Advanced Research and Reports*, **14(3)**, 22–29. <https://doi.org/10.9734/AJARR/2020/v14i330334>